Creep of CarbFix Basalt: Influence of Rock-fluid Interaction

Tiange Xing[1], Hamed O. Ghaffari[1], Ulrich Mok[1], Matej Pec[1]

[1]Department of Earth, Atmospheric and Planetary Sciences, Massachusetts Institute of Technology

Correspondence to: Tiange Xing (tiange@mit.edu)

Abstract. Geological carbon sequestration provides permanent CO_2 storage to mitigate the current high concentration of CO_2 in the atmosphere. CO_2 mineralization in basalts has been proven to be one of the most secure storage options. For successful implementation and future improvements of this technology, the time-dependent deformation behavior of reservoir rocks in presence of reactive fluids needs to be studied in detail. We conducted load stepping creep experiments on basalts from the CarbFix site (Iceland) under several pore fluid conditions (dry, H_2O-saturated and H_2O+CO_2-saturated) at temperature, T≈80°C and effective pressure, P_{eff} = 50 MPa, during which we collected mechanical, acoustic and pore fluid chemistry data. We observed transient creep at stresses as low as 11% of the failure strength. Acoustic emissions (AEs) correlated strongly with strain accumulation, indicating that the creep deformation was a brittle process in agreement with microstructural observations. The rate and magnitude of AEs were higher in fluid-saturated experiments than in dry conditions. We infer that the predominant mechanism governing creep deformation is time- and stress-dependent sub-critical dilatant cracking. Our results suggest that the presence of aqueous fluids exerts first order control on creep deformation of basaltic rocks, while the composition of the fluids plays only a secondary role under the studied conditions.

1 Introduction

The concentration of atmospheric CO_2 has seen a significant increase over the last century, raising concerns about the more frequent occurrence of extreme weather, sea-level rise and the projected increase of average global temperature (Broecker, 1975). It is estimated that about 800 Gt CO_2 will need to be stored by the end of the century to keep the global temperature increase below 1.5 ˚C compared to pre-industrial levels (National Academies of Sciences, Engineering, 2019). Such large volumes can practically be stored in the sub-surface. Geological carbon sequestration (GCS) by in-situ carbon mineralization is recognized as one of the most secure, long-term storage solutions (Gislason and Oelkers, 2014; Kelemen and Matter, 2008; Lackner et al., 1995; Mani et al., 2008; Seifritz, 1990; Snæbjörnsdóttir et al., 2020; Tutolo et al., 2021). To date, several pilot projects have been launched to study GCS in basalt reservoirs, including the CarbFix program in Iceland (Callow et al., 2018; Gislason et al., 2010; Oelkers et al., 2008; Snæbjörnsdóttir et al., 2018) and the Wallula basalt (part of Columbia River Basalt Group) sequestration project in Washington, US (McGrail et al., 2006, 2011, 2017; Zakharova et al., 2012).

GCS involves the injection of fluids, either supercritical CO_2 or CO_2 in an aqueous solution, into the formations. Basalts are composed of mafic minerals such as pyroxene ($(Mg,Fe)_2Si_2O_6$), plagioclase ($(Ca,Na)Al_{1.70}Si_{2.30}O_8$), and olivine ($(Mg,Fe)_2SiO_4$) as well as mafic glass, which react with CO_2 to form carbonate minerals (e.g $MgCO_3$, $CaCO_3$, $FeCO_3$ etc.), thus binding the injected CO_2 in mineral structure (Gislason and Hans, 1987; Hangx and Spiers, 2009;

Matter et al., 2007; Oelkers et al., 2008). Carbonation reactions appear to be rapid in natural conditions; more than 95% of the CO_2 injected into the CarbFix site in Iceland was converted to carbonate minerals in less than 2 years (Matter et al., 2016). Relevant fluid and mineral reactions can be formulated as follows (Hangx and Spiers, 2009; Hansen et al., 2005; Kelemen and Matter, 2008; Oelkers et al., 2008):

Dissociation:

$$CO_2 + H_2O \rightleftharpoons H_2CO_3 \qquad\qquad (Eq.\,1)$$

$$H_2CO_3 \rightleftharpoons HCO_3^- + H^+ \qquad\qquad (Eq.\,2)$$

Dissolution:

$$(Mg,Fe)_2Si_2O_6 + 4H^+ = 2(Mg,Fe)^{2+} + 2SiO_2 + 2H_2O \qquad\qquad (Eq.\,3)$$

$$CaAl_2Si_2O_8 + 8H^+ = Ca^{2+} + 2Al^{3+} + 2SiO_2 + 4H_2O \qquad\qquad (Eq.\,4)$$

$$(Mg,Fe)_2SiO_4 + 4H^+ = 2(Mg,Fe)^{2+} + SiO_2 + 2H_2O \qquad\qquad (Eq.\,5)$$

Precipitation:

$$(Mg,Ca,Fe)^{2+} + HCO_3^- = (Mg,Ca,Fe)CO_3 + H^+ \qquad\qquad (Eq.\,6)$$
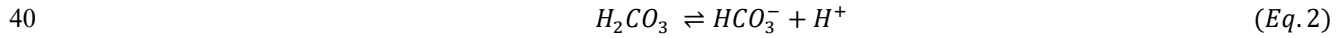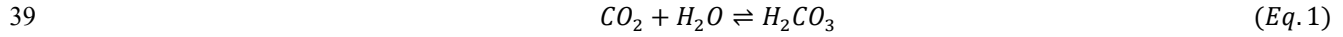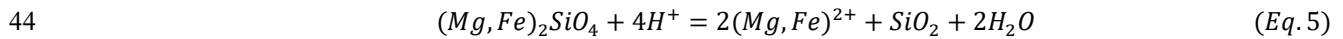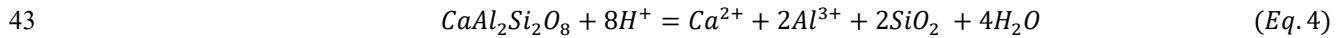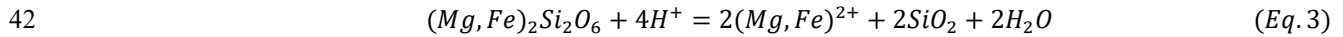
CO_2 is dissolved in water to form an acidic solution (Eq. 1-2). The rocks dissolve to liberate divalent cations (Eq. 3-5), which upon saturation in the fluid, precipitate as carbonate minerals (Eq. 6) further downstream from the injection site.

The mechanical and transport behavior of rocks can be significantly affected during GCS by the interaction between rock and fluid, both from a mechanical as well as chemical perspective (Baud et al., 2000; Dunning & Miller, 1985; Heard, 1960; Helmons et al., 2016; Rutter & Hackston, 2017). The mechanical effect of pore fluid is readily accounted for by using the effective pressure law (Terzaghi, 1943). The pore fluid acts against the normal stresses acting on crack surfaces hence reducing the shear stress necessary to overcome internal friction of the rocks. Increase in pore pressure during injection can trigger seismicity and therefore pore pressure has to be carefully monitored (Atkinson et al., 2020; Guglielmi et al., 2015). In addition to this mechanical effect, a number of chemical processes can occur in the presence of reactive fluids, leading to complex coupling between processes. For example, the replacement of mafic minerals with carbonates can result in an up to ~44% increase in solid molar volume (Goff and Lackner, 1998; Hansen et al., 2005; Kelemen and Matter, 2008) potentially clogging pore space, reducing permeability and increasing pore pressure. Alternatively, this volume expansion can generate stresses causing reaction-induced fracturing, which provides additional fluid pathways and maintains porosity and permeability for the reaction to proceed (Iyer et al., 2008; Jamtveit et al., 2009; Kelemen & Matter, 2008; Lambart et al., 2018; Macdonald & Fyfe, 1985; Renard et al., 2020; Rudge et al., 2010; Skarbek et al., 2018; Xing et al., 2018; Zhu et al., 2016). The fracturing behavior itself is affected by the fluid chemistry via kinetic reduction of fracture energy due to fluid absorption on mineral surfaces and crack tip blunting (Baud et al., 2000; Orowan, 1944; Rutter, 1972; Scholz, 1968), and activation of fluid-promoted stress corrosion processes such as subcritical crack growth resulting in time-dependent deformation, which is the focus of

67   this paper (Anderson & Grew, 1977; Atkinson, 1984; Atkinson & Meredith, 1987; Brantut et al., 2013; Nara et al.,

68   2013; Rice, 1978).

69   This time-dependent deformation, often called "brittle creep" or "static fatigue", has been observed in all types of

70   rocks tested to date (Atkinson & Meredith, 1987; Brantut et al., 2012; Heap et al., 2011; Kranz et al., 1982; Robertson,

71   1960; Scholz, 1968; Zhang et al., 2012). During brittle creep, flaws such as micro-cracks contained in natural rocks

72   are sub-critically stressed and propagate slowly due to stress corrosion (a chemical weakening process) at crack tips

73   in the presence of fluids. Sample-scale fracture then occurs after some time delay when the cracks coalesce and reach

74   a critical length. As a result, the rocks lose their load bearing capabilities and fail along a macroscopic fault plane at

75   stresses well below their short term strength (Scholz, 1972). For the sake of simplicity, we will use creep in the

76   following text to refer to this brittle creep deformation.

77   It has been shown by experiments, observations and modelling that stress corrosion is the dominant mechanism of

78   subcritical crack growth in rocks under upper crustal conditions (Brantut et al., 2012; Michalske and Freiman, 1983;

79   Reber and Pec, 2018). Brittle creep deformation can be accelerated due to changes in the rate of stress corrosion

80   induced by the chemistry of the injected fluids (Renard et al., 2005, 2020) or decelerated by crack tip blunting due to

81   fluid interaction (Scholz, 1968). Overall, it is hypothesized that changes in stress corrosion crack growth rate due to a

82   change in fluid chemistry will be reflected in similar changes of the macroscopic creep strain rate, either accelerating

83   or decelerating based on the details of the ongoing dissolution – precipitation reactions (Brantut et al., 2013). Hence,

84   the effect of CO_2-rich fluids needs to be quantified for GCS applications.

85   To summarize, the influence of rock-fluid interaction on deformation is complicated and includes the coupled effects

86   of mineral dissolution and precipitation, kinetics of fluid assisted deformation and injection pressure built-up, finally

87   resulting in time-dependent rock deformation. Carbonation changes the bulk composition of the basalts, alters their

88   strength and pore structure, and affects the permeability of the rocks (Dunkel et al., 2017; Kanakiya et al., 2017;

89   Kelemen et al., 2013; Kelemen & Hirth, 2012; Lisabeth et al., 2017; Xing et al., 2018; Zhu et al., 2016). Understanding

90   of the effects of rock-fluid interaction on deformation requires dedicated laboratory studies with diverse fluid

91   compositions at in-situ pressure conditions and at elevated temperatures acting over extended timescales. The present

92   study aims at elucidating the effect of rock-fluid interaction on the time-dependent rock deformation by investigating

93   long-term creep of Iceland Basalt saturated with various fluid compositions.

94   2 Materials and Methods

95   2.1 Starting Material and Sample Configuration

96   We used Iceland Basalt drill cores from the CarbFix site, collected at ~350 m depth. The composition of Iceland Basalt

97   has been identified as tholeiite and contains ~ 25 wt% of calcium, magnesium and iron oxides (7-10 wt% Ca; 5-6 wt%

98   Mg; 7-13 wt% Fe) with an average porosity of ~ 8% based on hydrological and tracer recovery modeling (Alfredsson

99   et al., 2008, 2013; Aradóttir et al., 2012; Matter and Kelemen, 2009; Snæbjörnsdóttir and Gislason, 2016). The rock

100   is formed by an aphanitic matrix that consists of crystals of feldspars, clinopyroxene, olivine, glass and secondary

101   alteration minerals as shown in Figure 1 and A1. Our observations are consistent with previously reported petrographic

102   analysis which shows that the primary minerals of the Iceland Basalt are predominantly plagioclase (An90-30), olivine

103   (Fo90-80), clinopyroxene (augite), magnetite-ilmenite, and interstitial glass, alteration of the basaltic lava flows

104   commonly leads to smectite and zeolite precipitation (Alfredsson et al., 2013; Larsson et al., 2002). The fraction of

105   crystal-to-glass ratio as well as crystal habitat is variable as documented in Figure 1. Round pores with a mean diameter

106   of ~ 0.5 mm are randomly distributed throughout the matrix, some are filled with feldspar (primarily potassium

107   feldspar) and some are voids with no filling (Figure 1). Pore-, as well as pre-existing crack-walls are coated by a thin

108   layer of a phyllosilicate as documented in Figure 1d and 1e. The matrix is locally altered by dissolution of larger

109   subhedral feldspar crystals and local replacement by phyllosilicate (see Figure 1b and 1e). Cylindrical samples were

110   ground to ~ 40 mm in diameter and ~ 80 mm in length (see Table 1). The samples were jacketed using copper foil of

111   ~0.05 mm thickness, joined to titanium end-caps by Viton tubes and coated with Duralco 4538 epoxy. The end-caps

112   had a concentric hole which allows fluid access to the sample. Figure 2 shows the schematics of the sample

113   configuration in this study. An internal force gauge was mounted below the sample inside the vessel, allowing direct

114   measurement of the differential stress ($\Delta\sigma = \sigma_1 - \sigma_3$). Displacement of the axial piston was measured externally using

115   a linear variable differential transformer (LVDT). Variations of the sample length were measured using two internal

116   LVDTs. Local axial (ϵ_a) and radial strains (ϵ_r) of the rock were measured using strain gauges affixed to the copper

117   jacket around the sample. Piezoelectric sensors were installed around the sample for passive monitoring of acoustic

118   emissions (AE).

119
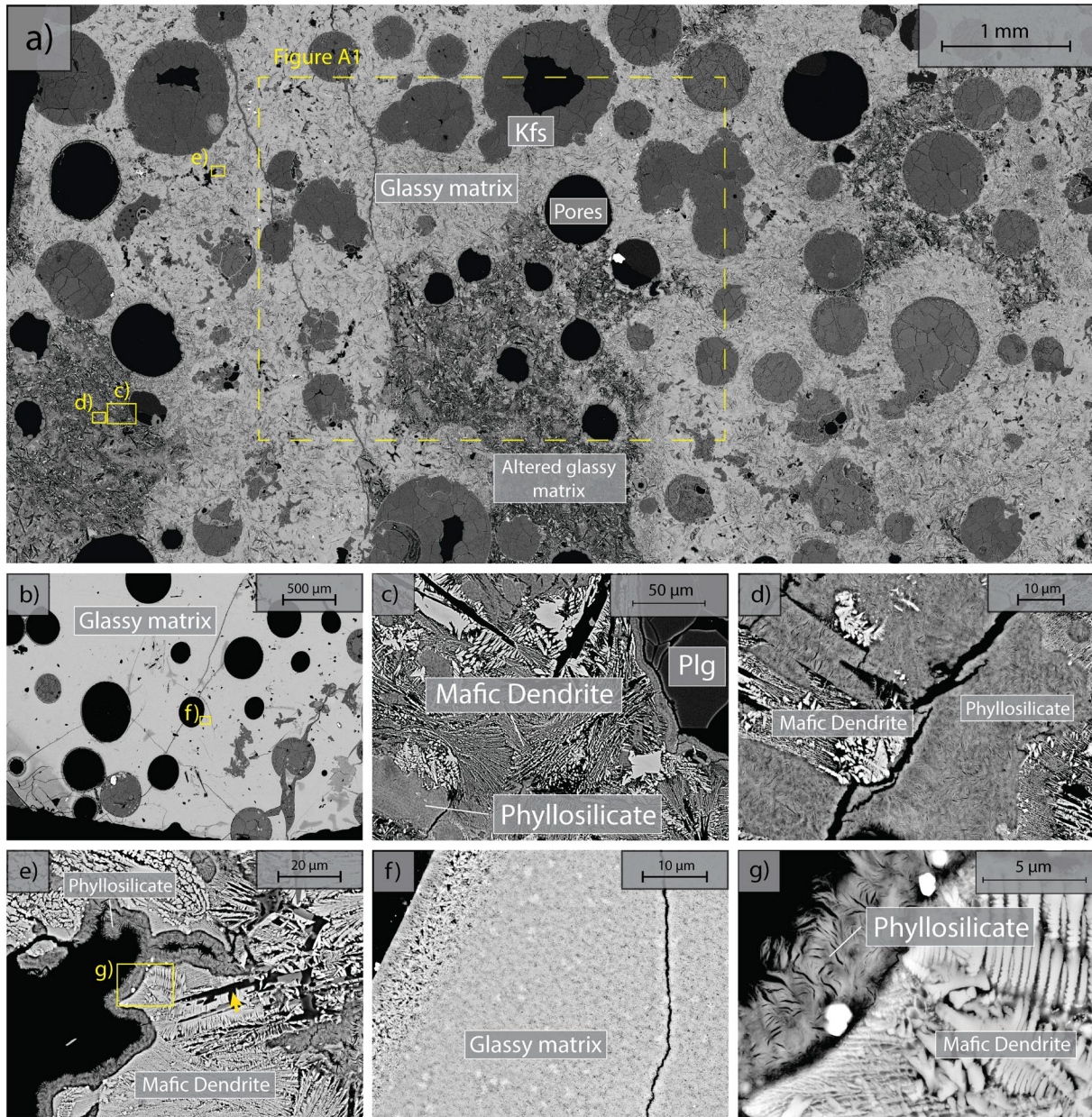
Figure 1. Backscattered electron (BSE) images of the starting material. Location of higher-magnification images is shown by yellow rectangles a) Representative sample microstructure; Glassy matrix shows a range of crystal content and habitat and is locally altered; Area where Energy Dispersive Spectroscopy (EDS) analysis is conducted (see details in Appendix Figure A1) is marked by the dashed rectangle; b) Another common glassy matrix microstructure with finer, more homogenous crystals; c) Detail of altered matrix and pore wall. Note black voids in the shape of subhedral feldspar laths in the matrix; d) Detail of patchy phyllosilicate alteration and dendritic crystals in altered matrix; e) high-magnification image of dendritic crystals forming the matrix and phyllosilicate coating of the pore wall; f) high magnification image of glassy matrix with homogenous small crystals g) high-magnification image of dendritic crystals forming the unaltered matrix and high magnification image of the phyllosilicate alteration.

Because of the variation in structure and composition of the natural material and limited drill core material available, we adopted the 'stress-stepping' experimental procedures to study creep deformation (Heap et al., 2009; Lockner, 1993). This method allows several creep experiments to be conducted on a single sample at different stress levels and

132   minimizes the issue of inter-sample variability (see details in Section 2.2). Piezoelectric sensors allowing independent

133   recording of compressional and shear waves were fabricated with PZT-5A ceramics with thickness of 3 to 5 mm and

134   resonance frequency of ~450 kHz to 1 MHz. The PZT-5A crystals were mounted on titanium spacers with one side

135   concavely curved to match the sample surface, thus providing protection of the sensing crystals and optimal contact

136   area. A back-up element was epoxied to the back of the sensor to minimize ringing. We also used analog low pass

137   filters (~500 kHz) compatible with the frequency range of the employed PZT ceramics to reduce the electromagnetic

138   interference (EMI) effect. Data was collected using two combined 4-channel universal serial bus (USB) oscilloscopes,

139   recording at 50 MS/s with a 12-bit resolution (TiePie HS4-50). Using low noise amplifiers (ITASCA-60dB), we

140   carefully selected the most sensitive sensor positions, preferably far from each other, as master channels. The data

141   collection system was set such that, if the master channels detected a signal satisfying a sufficiently large signal/noise

142   ratio in a moving time window, the event would be recorded in all channels. We amplified the two master channels

143   with a flat gain of 60 dB in a frequency range of 50 kHz to 1.5 MHz. Frequencies from 1.5 MHz to 15 MHz were

144   amplified nonlinearly, the gain decreasing exponentially from 52 dB to 37 dB with increasing frequency (Ghaffari et

145   al., 2021; Ghaffari and Pec, 2020). Considering the above limitations, the main frequency range of the recording

146   system was between ~50 and 500kHz, although other frequencies could be recorded owing to the exponential nature

147   of the amplification filters.
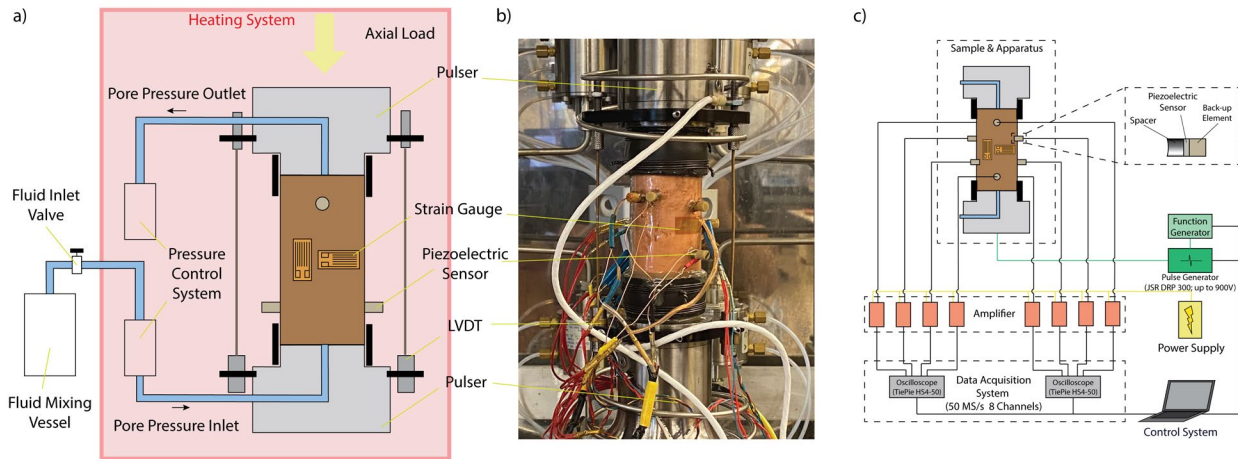
148

149   **Figure 2**. a) Schematics of sample configuration. The whole sample assembly and pore fluid actuators are enclosed
150   in a servo-controlled heating system to ensure a uniform temperature condition; b) Photo of the sample assembly; c)
151   Illustration of the acoustic emission recording system.

152

153   All experiments were conducted at 50 MPa effective pressure, P_{eff}, with pore fluid pressures, P_f, of either 0 or 5 MPa
154   for dry and fluid-saturated experiments, respectively. The fluids used in this study were H_2O and H_2O+CO_2. The
155   H_2O+CO_2 fluid is prepared in the fluid mixing vessel (Figure 2a) where deionized water is saturated with CO_2 in the
156   vessel under a gas pressure of 5 MPa. The fluid-saturated samples were first immersed in deionized water under
157   vacuum for more than 30 days prior to the experiment. Details of the experimental conditions are listed in Table 1.
158   The samples were inserted in the NER Autolab 3000 testing rig installed at MIT and deformed under tri-axial stress
159   conditions, with the maximum principal stress (σ_1) acting in the axial direction. The radial principal stresses (σ_2 and
160   σ_3) were generated by the confining pressure, i.e., $\sigma_2 = \sigma_3 = P_c$. The effective pressure is calculated as $P_{eff} = P_c - P_f$.
161   During deformation, a constant pressure difference of 0.5 MPa was maintained between the inlet and outlet of the pore

162 pressure system, while the mean pore pressure was kept at 5 MPa. We thus maintained fluid flow across the sample
163 and measured the permeability evolution during deformation. In one H_2O+CO_2 experiment (OR2_M), we closed the
164 fluid mixing vessel after the initial filling of the sample and thus formed a close pore fluid loop (OR2_M was referred
165 to as H_2O+CO_2 close experiment in the following discussion). In the other H_2O+CO_2 experiment (OR3_B), the pore
166 fluid system was connected to the fluid mixing vessel during the entire experiment and therefore acted as a semi-open
167 system since it was in constant communication with a large CO_2 source (OR3_B was referred to as H_2O+CO_2 open
168 experiment in the following discussion).

Experiment Number	Sample Length (mm)	Sample Diameter (mm)	Confining Pressure (MPa)	Pore Pressure (MPa)	Effective Pressure (MPa)	Pore Fluid Composition	Temperature (˚C)	Young's Modulus (GPa)	Failure Strength (MPa)	Strain at Failure (%)	Initial Porosity (%)
OR5	77.37	39.32	50	0		-		17.6	>105	1.89	15
OR2_T	81.5	38.01	55	5		H_2O		12.1	72	1.71	11
OR2_M	81.48	39.22	55	5	50	$H_2O + CO_2$	78	16.2	55	0.84	5
OR3_B	77.94	39.81	55	5		$H_2O + CO_2$		28.0	130	2.00	-

169 **Table 1.** Details of the sample parameters and experimental conditions. Sample OR5 was not loaded to its failure
170 strength due to early failure of the strain gauges and LVDTs. Porosity is estimated from the X-ray tomographic image
171 of the sample. Initial porosity of the sample OR3_B is not available due to limited access to the X-ray tomography
172 facility during COVID-19 pandemic.

173 We started the experiments by bringing the sample to an effective pressure of 50 MPa and subsequently to a
174 temperature of ~80˚C while holding the pressure constant. Heating the sample took ~12 hours, long enough to allow
175 thermal equilibrium to be reached. After reaching the desired P - T conditions, the samples were deformed using a
176 step loading procedure. During a step, the differential stress was increased at a rate of ~2 MPa/min, which corresponds
177 to an axial strain rate of ~1.1×10^{-6} s^{-1}. Once the desired stress level was reached, we kept the load constant for ~24
178 hours, while monitoring the sample deformation. This step sequence was repeated until failure of the sample occurred
179 – typically during the increase of differential stress. We recorded the stress level at which the failure occurred as
180 'failure strength' and use this parameter to quantify the strength of the tested material. We point out that the definition
181 of 'failure strength' used here presents a lower bound for the commonly presented 'ultimate strength' which is
182 measured in short-term, constant displacement rate deformation experiments. The dry experiment is halted earlier due
183 to failure of the strain gauges and LVDTs and therefore the strength estimate is only a lower bound of the failure
184 strength. The total duration of the experiments ranged between 5 to 12 days. Details of the load steps are summarized
185 in Appendix (Figure A2).

186 In this study, we focus on the transient creep evolution and only creep steps where final failure is not observed are
187 analyzed. We use the term phase I to refer to the creep immediately following a stress change, during which the creep
188 strain evolves rapidly (i.e., relatively higher strain rate). We call phase II the portion of the creep curve with an
189 approximately constant or very slowly varying strain rate over a ~24h window (i.e. $d\varepsilon/dt = cte$.; see Appendix
190 Figure A3). For comparison with previous work on brittle creep, we calculate a characteristic creep strain rate using a
191 least-squares fit to the slope of the creep strain vs. time curve during the identified phase II transient creep (Appendix
192 Figure A5; we will simply refer to it as creep rate in the following discussion).

193 To investigate the micro-structural changes occurring during deformation, the rock samples were scanned before and
194 after deformation using X-ray computed tomography with scan parameters set at ~150 kV and ~250 µA. The obtained
195 X-ray images have a pixel size of ~90×90 µm. Thin sections were prepared from selected samples and imaged using
196 a field emission scanning electron microscope (SEM).

197 The evolution of fluid composition was evaluated by collecting fluid samples from the end of the pore fluid outlet
198 (Figure 2a) after each creep step. The concentration of Mg^{2+}, Ca^{2+} in the fluid sample were analyzed using the
199 Inductively Coupled Plasma Mass Spectrometry (ICP-MS).

200 **3 Results**

201 **3.1 Creep Deformation and Creep Strain Rate**
202 The creep deformation during each load step exhibited typical transient creep evolution (Brantut et al., 2013;
203 Robertson, 1964; Scholz, 1968) with a transition from phase I where rapid straining occurs to a slowly varying phase
204 II which exibits an approximately constant strain rate over our observation time (Figure 3). This transition generally
205 took place within the first 10^4 s (~2.7 hrs) of the loading step. In the dry experiment, large variations in phase I creep
206 strains were observed (Figure 3a & 4c) and the creep rates measured during the slowly evolving phase II stages showed
207 a neutral sensitivity to stress (Figure 3e). In experiments where pore fluids were present (H_2O and H_2O+CO_2), the
208 strain accumulated during the phase I creep systematically increased with increasing stress and the creep strain rate
209 during the phase II creep displayed a clear exponential dependence on stress (Figure 3e). This stress sensitivity of
210 creep strain rate showed strong similarity in the different experiments irrespective of the pore fluid composition and
211 can be adequately described by power law (e.g. Atkinson, 1984; Meredith and Atkinson, 1983) as well as exponential
212 functionals (Charles and Hillig, 1962; Hillig, 2006), but the exponential model seems to work slightly better with our
213 data according to the R^2 value (see Appendix Figure A6).

214
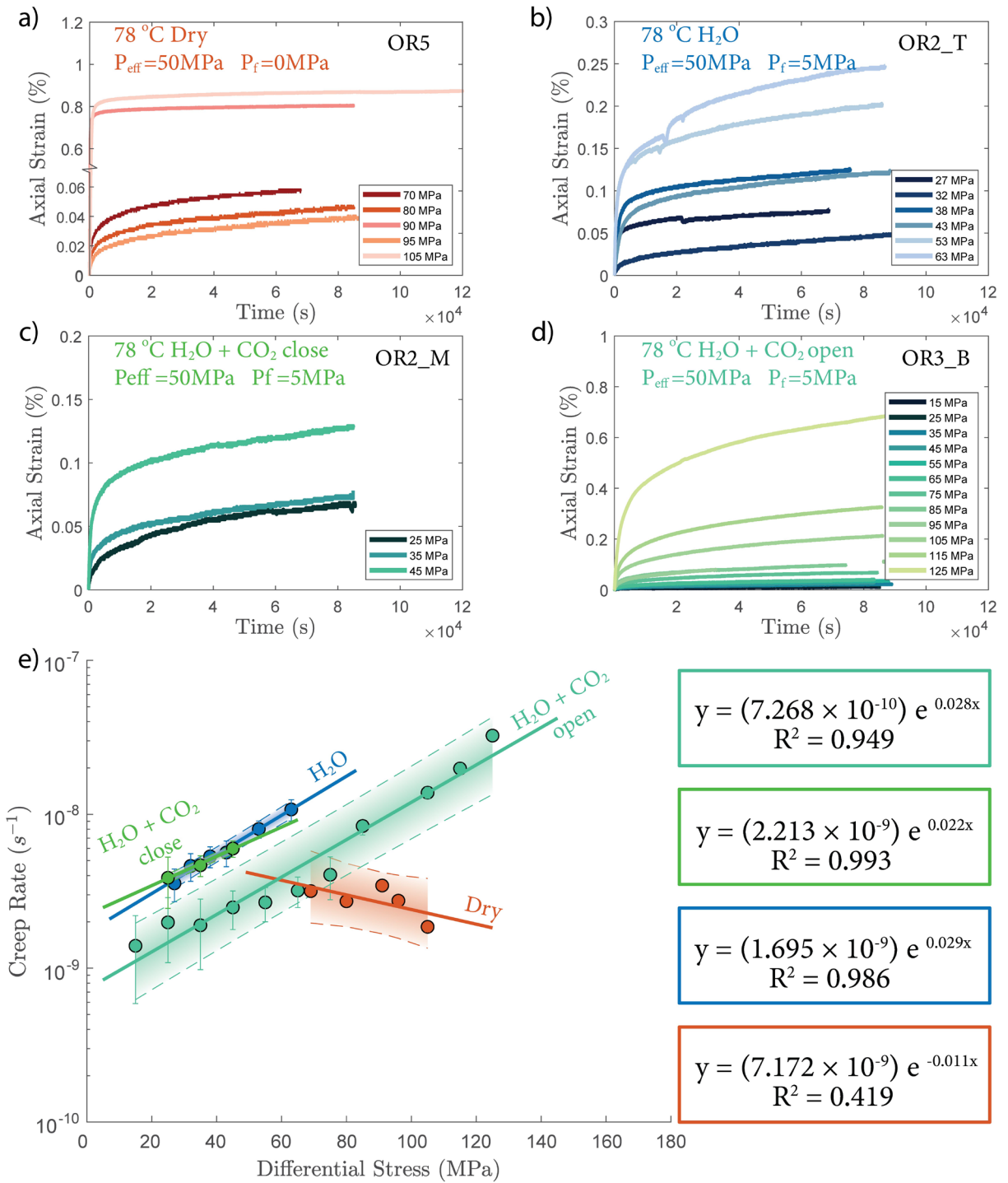
Figure 3. a) - d) Axial strain evolution of each individual stress step for all experiments; e) Stress dependence of creep rate. The error bar marks the 95% confidence interval of each calculated creep rates. The stress-creep rate relationship can be best modeled using an exponential law. The dash line and shaded area marks the 95% confidence interval of the fitted exponential relationship. The stress dependence of creep rate in the dry experiment is considered neutral as the R^2 becomes low for the fitting with negative slope. Color code of the plot follows the same as a) - d).

220   In Figure 4 we compare the strain accumulation during phase I and II of the transient creep as illustrated in Figure

221   A4a. We observe a universal power-law relationship of the accumulated creep strain during phase I (ε_i) to creep stain

222   accumulated during phase II (ε_{ii}) in all experiments irrespective of fluid presence or the composition of the fluid

223   (Figure 4a), i.e. the ratio between $\log \varepsilon_i$ and $\log \varepsilon_{ii}$ remains constant. The accumulated creep strains during both phase

224   I and phase II were exponentially dependent on creep stress (Figure 4c and 4d). In Figure 4b we show that regardless

225   of the creep stress level, the ratio between the logarithmic accumulated phase I and logarithmic phase II creep strain

226   after ~24 hrs was approximately constant, except for two outliers associated with two stress steps in the dry

227   experiment, during which anomalously large phase I creep strains occurred (Figure 4a and 4c).

228   Overall, the fluid saturated samples crept faster than the dry sample during phase II stages in similar stress conditions.

229   In spite of variations in failurestrength, the fluid saturated samples consistently showed stronger stress dependence of

230   the creep rate than the dry sample. Comparing the fluid saturated experiments, we observe that the sample saturated

231   with H_2O had the same creep rate as the $H_2O + CO_2$ close experiment and a higher creep rate than the H_2O+CO_2 open

232   experiment under similar stress level. (Figure 3e). Analysis of the fluid chemistry demonstrates that the $H_2O + CO_2$

233   close and H_2O experiment show same fluid composition which we will describe in more detail in Section 3.6.

234
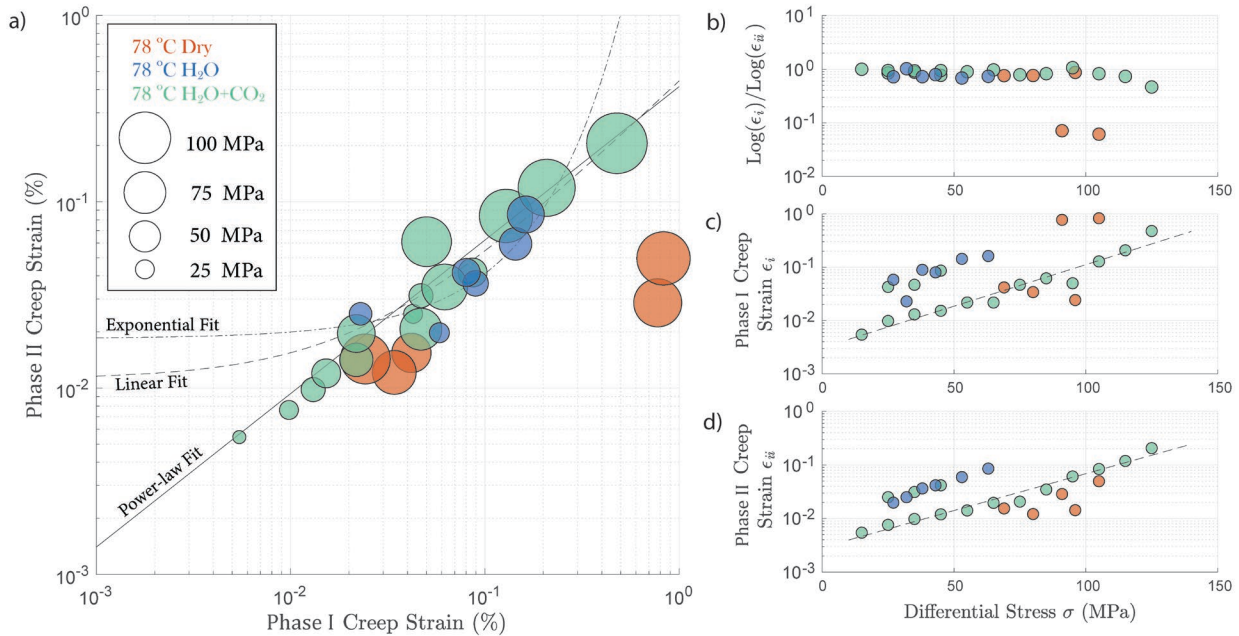
Figure 4. a) Relationship between total phase I creep strain and phase II creep strain ~24 hrs after the stress step
loading. The creep stress level is reflected by the size of the circles; b) ratio between the logarithmic total phase I and
logarithmic phase II creep strain remains constant and is independent of stress; the cumulated c) phase I and d) phase
II creep strain is exponentially dependent on the creep stress; The fitted lines are calculated based on the data obtained
from $H_2O + CO_2$ open experiment (OR3_M).

240   **3.2 Volumetric Strain**

241   In all experiments, creep deformation was initially compactive as indicated by a positive change in the volumetric

242   strain, ϵ_v, calculated from the strain gauge measurements ($\epsilon_v = \epsilon_a + 2\epsilon_r$). Shear-enhanced dilation (Brace et al., 1966)

243   started 10 - 20 MPa before the failure strength of the sample was reached (highlighted by yellow arrowheads in Figure

244   5). The onset of dilation generally occurred at lower stress level in the fluid saturated experiments than in dry

245   conditions. The largest dilation was observed in H_2O+CO_2 open experiments as shown in Figure 5d. In the dry

246   experiment, large amount of dilation ($\Delta\epsilon_v > 0.5\%$) was also observed at creep stress of ~90 MPa and ~105 MPa which

247   is significantly higher than in other steps ($\Delta\epsilon_v < 0.1\%$). Furthermore, the dilation at ~90 MPa is also accompanied by

248   a drop in stress (see Figure 5). The strength of the tested samples seems to be correlated with the elastic modulus

249   measurements, the stiffer the rock the higher the strength (see Table 1).
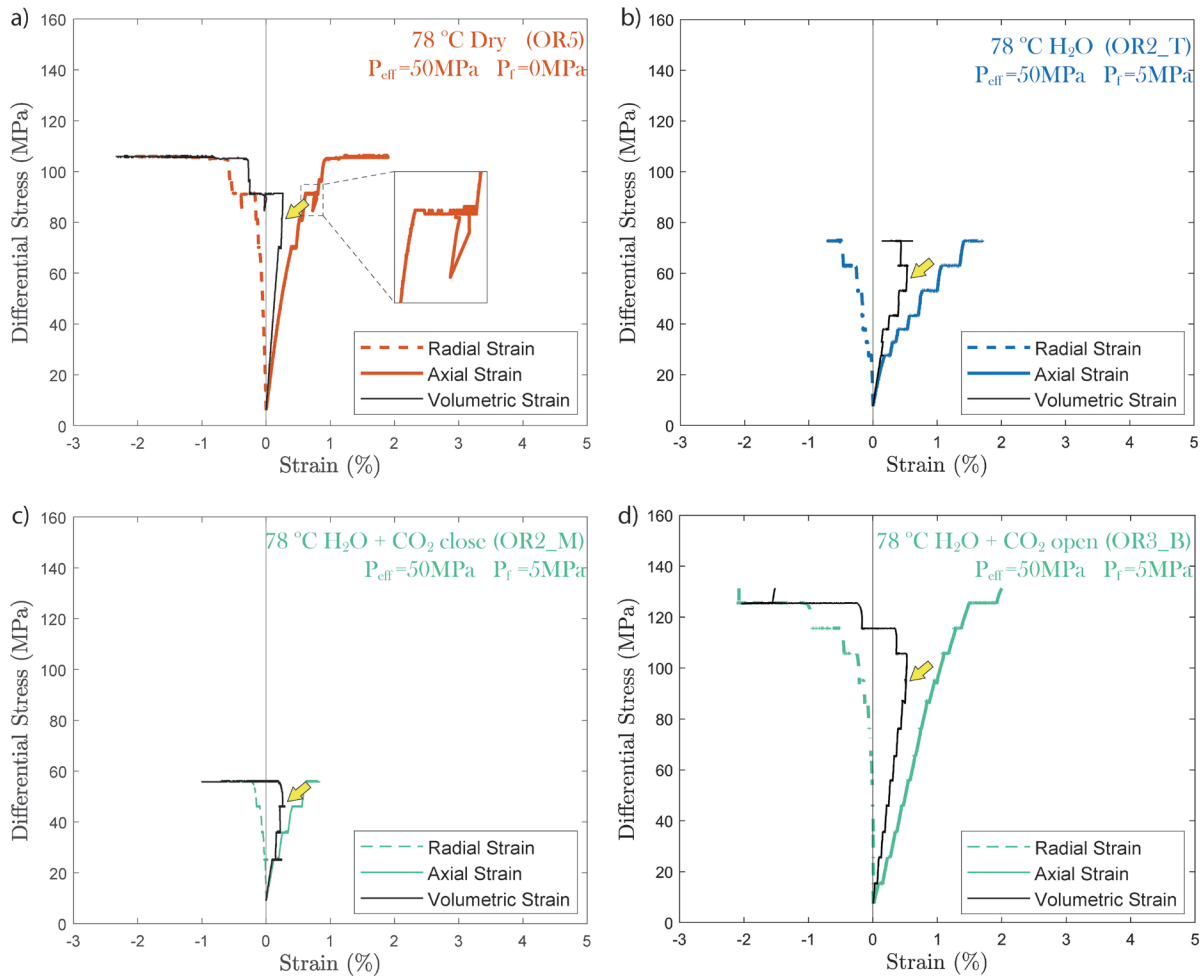
250

251   **Figure 5**. Plots of volumetric strain for a) dry, b) H_2O, c) H_2O+CO_2 close and d) H_2O+CO_2 open experiments. The
252   onset of transition from compaction to dilatancy (C*') is marked by the yellow arrowhead. In the dry experiment, the
253   differential stress exhibits temporary fluctuation at ~90 MPa (highlighted by the dashed rectangle).

254   **3.3 Permeability**

255   In fluid-saturated experiments, permeability decreased with increasing effective pressure during hydrostatic loading

256   (Figure 6a, b and c). The largest decrease in permeability was observed in the water-saturated experiment, where

257   permeability dropped by 3 orders of magnitude as effective pressure was raised from 15 to 50 MPa (Figure 6a).

258   Permeability reduction was much lower in both H_2O+CO_2 experiments, only ~ 1 order of magnitude, over the same

259   effective pressure range (Figure 6bc). Permeability variations after heating are shown in Figure 6d 6e and 6f, where

260 the minimum permeability reached during hydrostatic loading is indicated for comparison (empty circles in Figure 6d,
261 e and f). The permeability change during heating was rather small in the H_2O and H_2O+CO_2 close experiment, while
262 the H_2O+CO_2 open experiment exhibited more than an order of magnitude permeability reduction after heating.

263 During creep, permeability did not evolve much with time but did show a clear dependence with the stress level of the
264 individual creep stages, first slightly decreasing with increasing differential stress and then substantially increasing
265 when the onset of transition from compaction to dilatancy (C*') was passed, shortly before failure (Figure 6d and 6f).

266
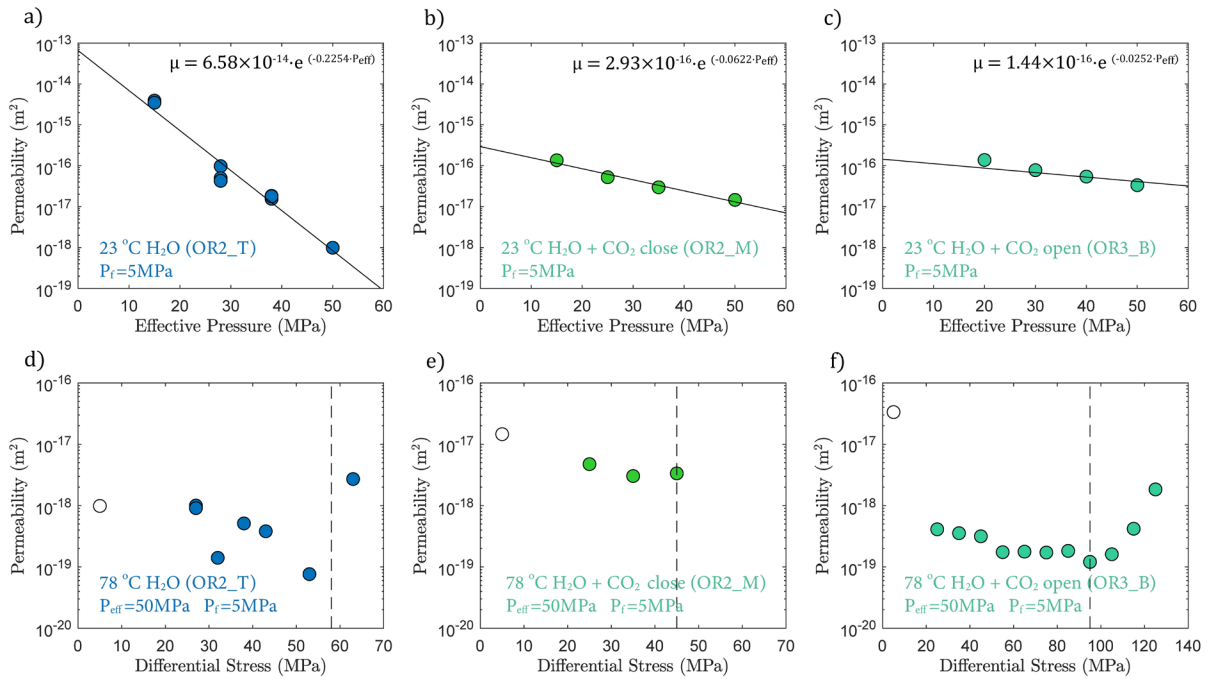
Figure 6. Permeability evolution due to changes in a) b) c) effective pressure and d) e) f) differential stress. The dash-line marks the onset of transition from compaction to dilatancy (C*') as previously shown in Figure 4. The empty circle indicates the permeability measurement before heating.

3.4 Characterization of the Acoustic Emissions

3.4.1 Passive Recording & Rate of AEs

272 We observed a strong correlation between acoustic emissions and mechanical data as documented in Figure 7. The
273 number and amplitude of AEs was substantially larger in the experiments with pore fluids than in the dry experiment,
274 irrespective of fluid composition. The rate of AEs increased during primary creep; the greater the accommodated
275 strain was, the higher the AE rate. The AE rate then decayed exponentially as the rock entered the later stage of the
276 transient creep. This decay was slower in all fluid saturated experiments where significant amount of AE activity
277 continued during the phase II creep stage. The AE rate increased as the stress was approaching the failure strength of
278 the sample (Figure 7). In Figure 8, we plot the normalized cumulative AE counts against the normalized creep strain
279 measured during each creep step. For all experiments with pore fluids, we see that the data-points tended to cluster
280 near the 0-1 diagonal (Figure 8b, c and d), thus supporting a strong correlation between acoustic emissions and creep

281 strain. In the dry experiment, most AEs occurred early in each load step (normalized strain ≤ 0.2) after which straining

282 continued with little AE activity (Figure 8a).

283
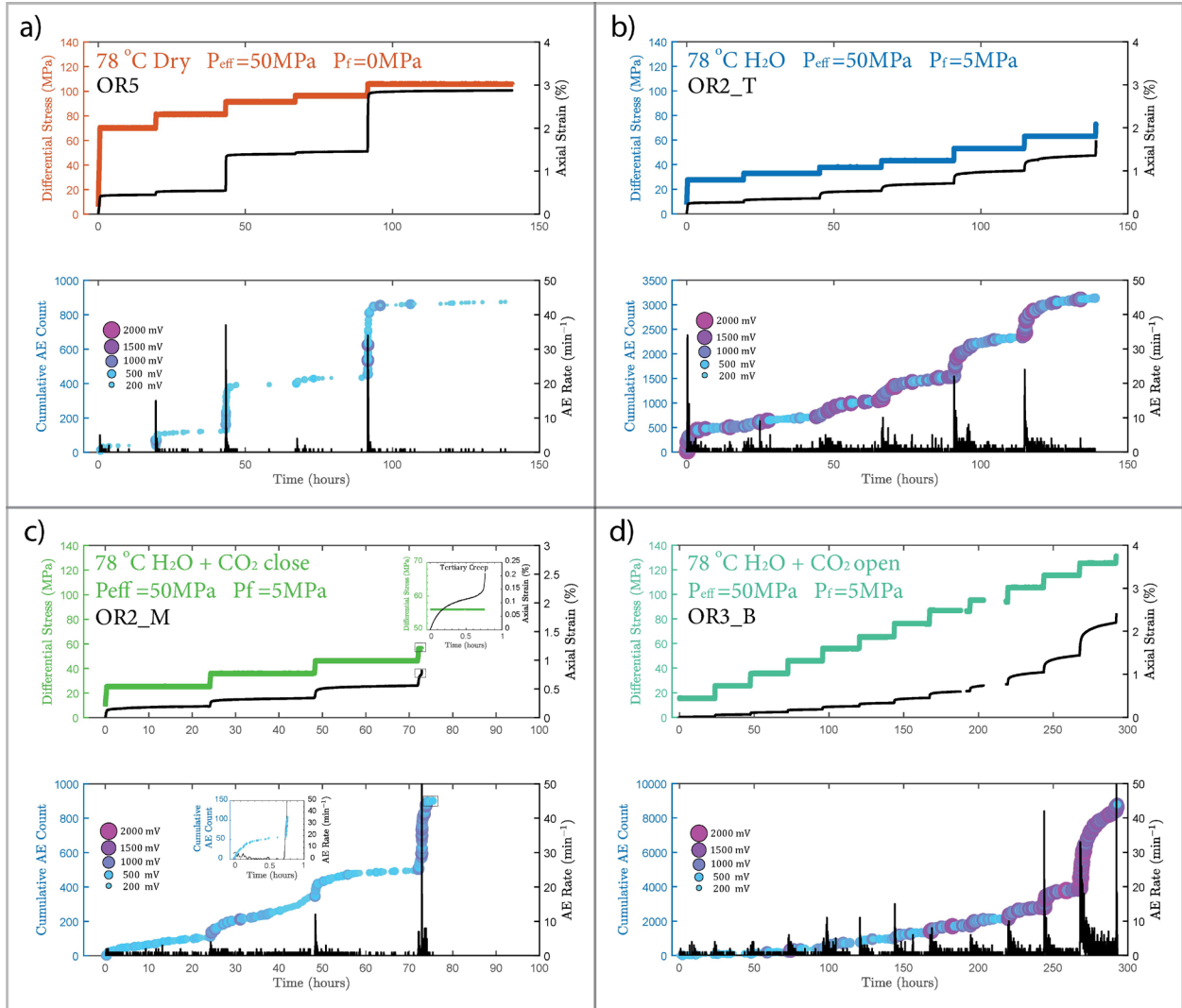
Figure 7. Top: Plot of stress loading steps and strain (black) evolution; Bottom: Evolution of cumulative number of acoustic emission (AE) and AE rate evolution (black) over time for a) dry, b) H$_2$O, c) H$_2$O+CO$_2$ close, note short tertiary creep stage accompanied by a burst of AE activities during the last stress step (see insets), d) H$_2$O+CO$_2$ open experiments.
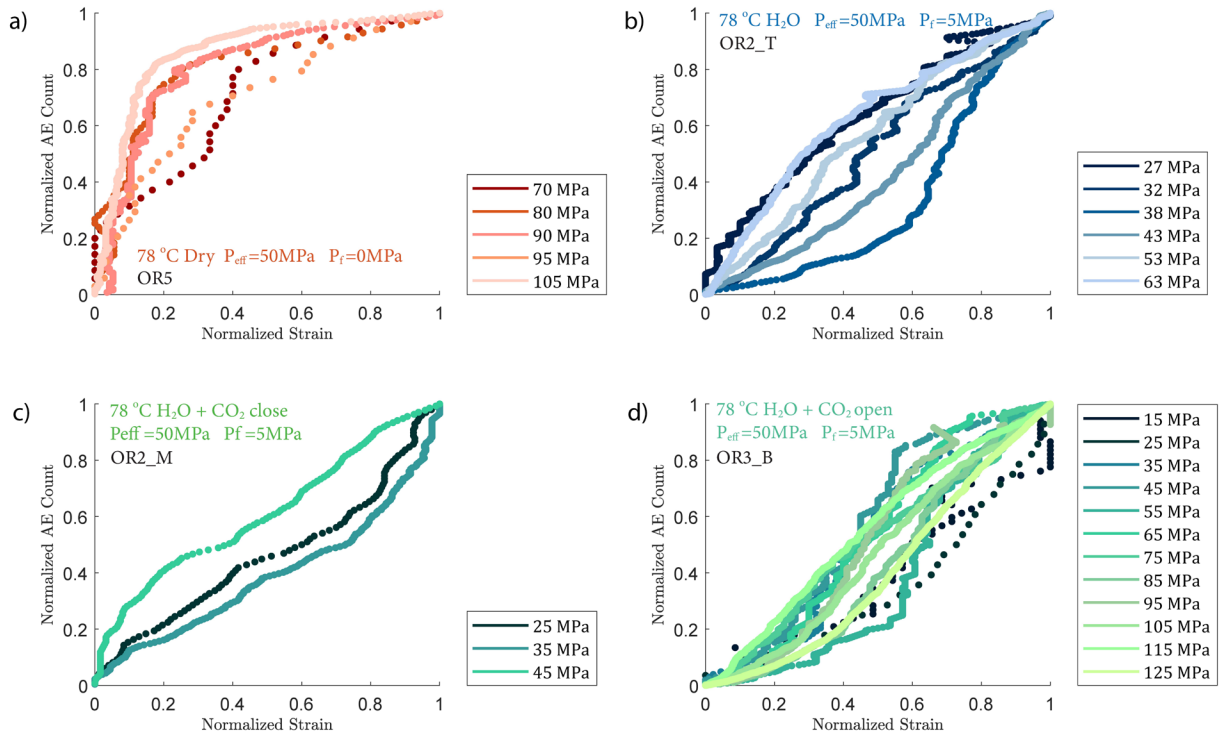
288
289 **Figure 8**. Plot of normalized cumulative AE count vs strain a) dry, b) H_2O, c) H_2O+CO_2 close and d) H_2O+CO_2 open
290 experiments. the normalized cumulative AE counts and strain during each creep step show an approximately linear
291 correlation in most cases except in the dry experiment.

292 **3.4.2 Gutenberg-Richter b-value**

293 The Gutenberg-Richter relationship provides a way to characterize the AE statistics for each creep step. The

294 Gutenberg-Richter *b*-value was calculated using the following equation:

295
$$\log N = a - b \log A \qquad\qquad (\text{Eq. } 7)$$

296 where A is the maximal amplitude of individual acoustic events and N is the number of events with magnitude larger

297 than A. Figure 9 shows that the *b*-value increased with increasing stress in the fluid saturated experiments but remained

298 constant in the dry experiment. The observed increases of the *b*-values indicate that low amplitude AEs had a

299 proportionally larger occurrence frequency with increasing stress.

300
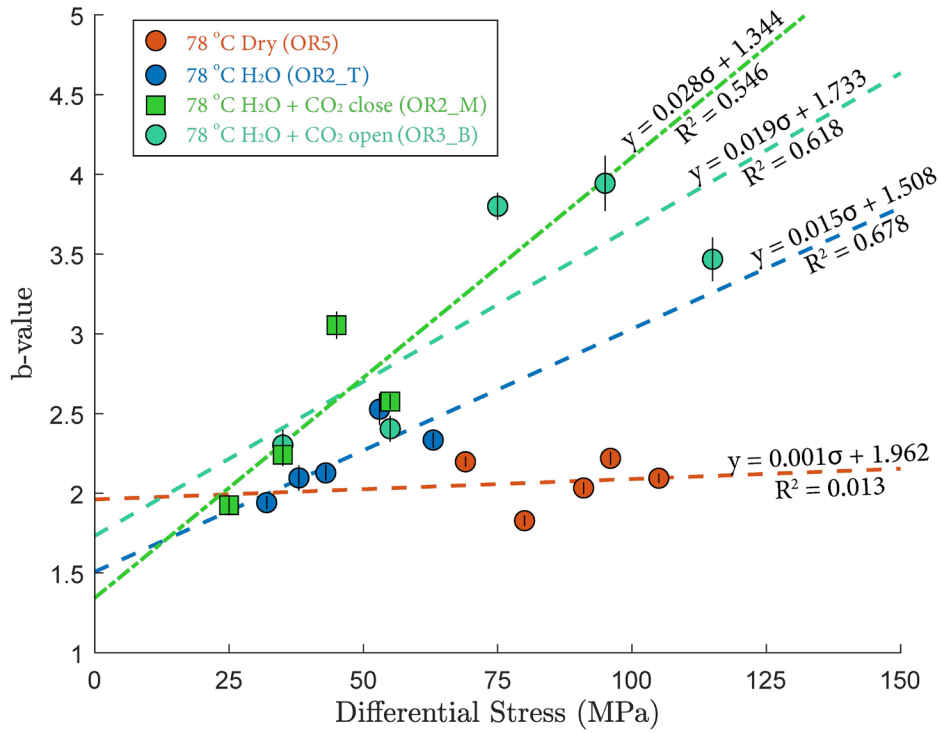
Figure 9. Differential stress dependence of Gutenberg-Richter *b*-values. See detailed b-value fitting in the Appendix
Figure A7. The error bar marks the 95% confidence interval of the calculated b-value.

3.5 Microstructure

Post-mortem examination of the samples reveals that fractures inside the fluid-saturated samples form a complex,

wide system rather than a clearly defined, distinct shear fault plane (Figure 10 and Appendix Figure A8). The fluid-

saturated samples exhibit bulging on the surface. In contrast, the dry sample shows a weakly developed fault plane

and less bulging, however it should be noted that this sample did not, in fact, reach failure strength.

H$_2$O + CO$_2$ (OR3_B)

a)   b)   c)

d)

50 mm
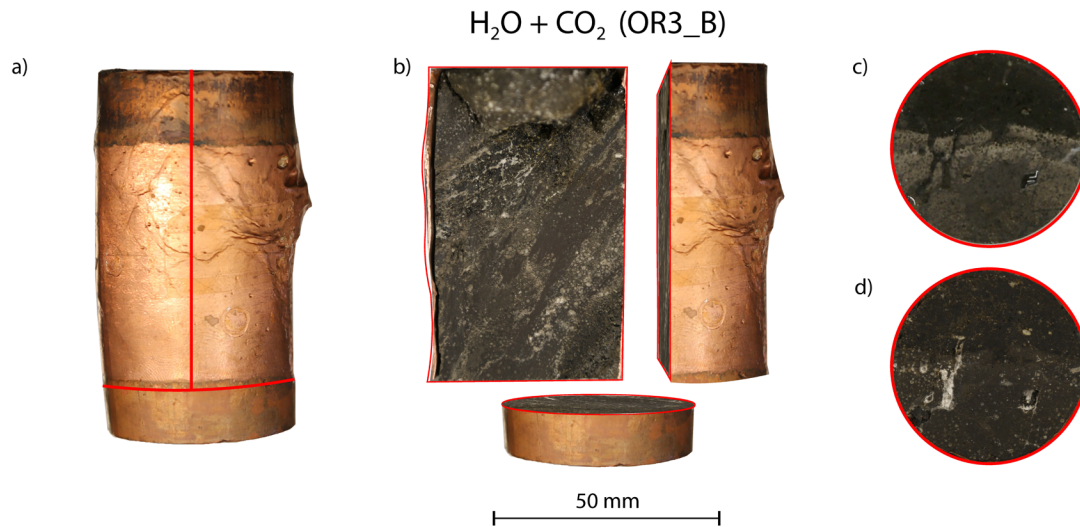
Figure 10. a) Deformed sample from H$_2$O+CO$_2$ open experiment (OR3_B). b) Cross-sectional view of the deformed sample. Top view of the sample c) before and d) after the experiment.

X-ray tomographic images (Figure 11) and BSE images (Figure 12) of the deformed samples display abundant fractures, whereas cracks are much more rare in the pre-deformation CT scans and the BSE images (Figure 1). The amount of visible cracks in each sample tends to scale with the cumulative AE count; the dry experiment has a lower fracture density than the experiments with H$_2$O and H$_2$O + CO$_2$ despite the fact that the dry sample experienced a higher stress and developed a larger total strain accumulation. To illustrate these observations, we selected representative pairs of 2D tomographic slices oriented parallel and perpendicular to the loading direction and traced the observable microcracks (Figure 11). We quantified both the orientation and anisotropy of the microcracks using the 'surfor' method that relies on the projection of an outline (Heilbronner and Barrett, 2014; Panozzo, 1984). As documented in Figure 11, cracks are strongly aligned in the axial sections. The cracks are mainly oriented parallel to the maximum principal stress in the H$_2$O+CO$_2$ experiment, indicating Mode I cracking, but are aligned 20~30˚ to the maximum principal stress in the dry and H$_2$O experiments, suggesting mixed Mode I + Mode II cracking. A weaker alignment is generally observed in radial sections.

3.6 Fluid Chemistry

Concentration of the Mg^{2+} and Ca^{2+} cations increased once heating started (Figure 13). This increase in the Mg^{2+} and Ca^{2+} concentration reflects the dissolution of Mg and Ca bearing minerals during the reaction. In the H$_2$O+CO$_2$ close experiment (OR2_M), the supply of CO$_2$ was limited and led to a dissolution dominated system that resulted in the high concentration of Mg^{2+} and Ca^{2+}, similar to the H$_2$O experiment (OR2_T). In the H$_2$O+CO$_2$ open experiment (OR3_B), the cation concentration was significantly lower than in the OR2_M and OR2_T experiments. This was likely caused by the potential precipitation uptake owing to the continuous supply of CO$_2$ in the semi-open setting of the pore fluid system. This interpretation is also supported by the ~2 orders of magnitude drop in permeability observed in the CO$_2$ open experiment after heating started since precipitation could potentially clog the pore throats and lead to permeability decrease.

333
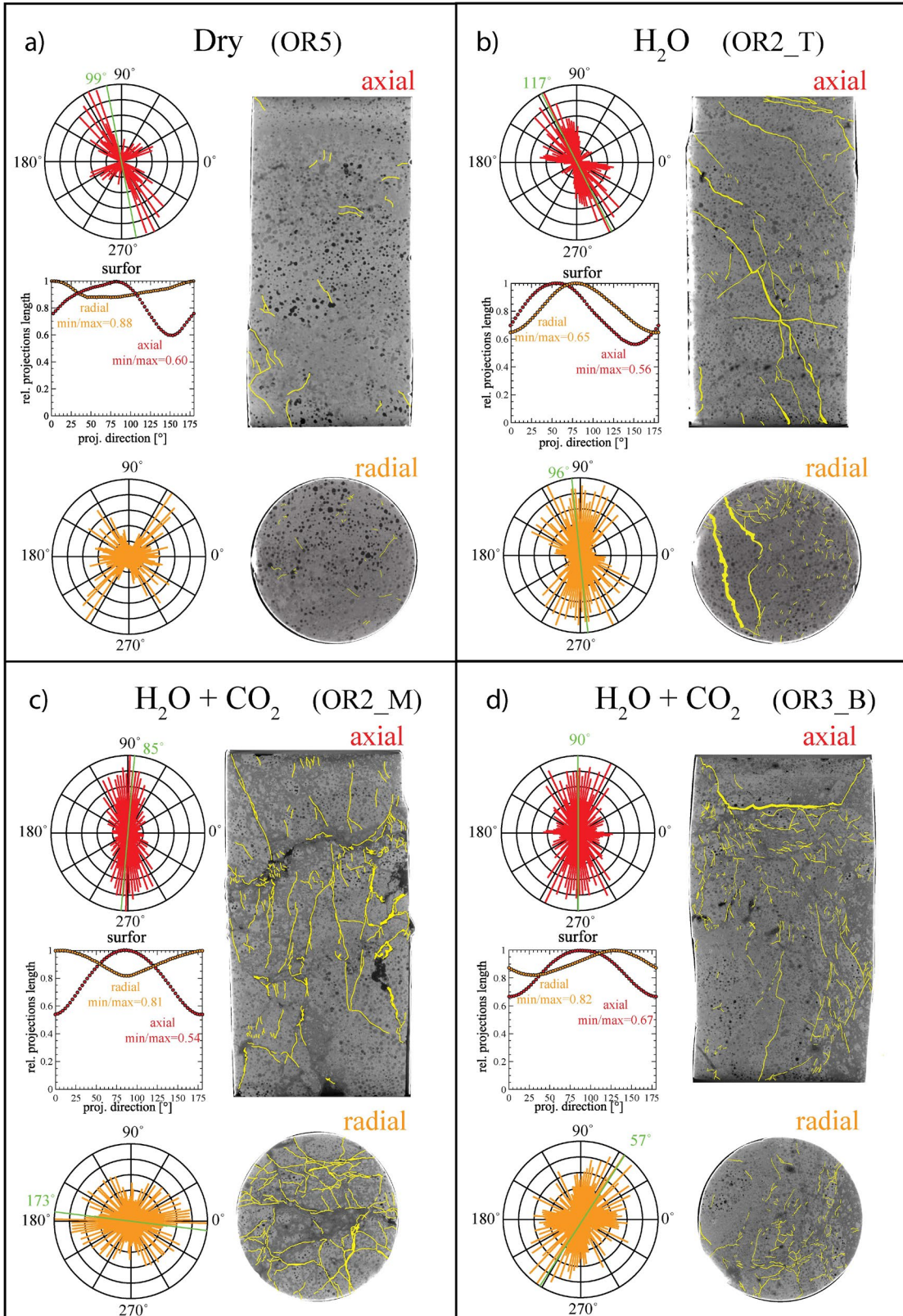
334 **Figure 11**. Orientation analysis of cracks in axial and radial directions from x-ray tomographic images of the deformed
335 sample from a) dry, b) H_2O, c) H_2O+CO_2 close and d) H_2O+CO_2 open experiments. The aspect ratio (min/max), which
336 is defined by the ratio between the minimum and maximum projection length of the cracks, is 1 when the orientation
337 is random (isotropic) (Heilbronner and Barrett, 2014). Strong crack alignment is inferred in the axial sections with
338 aspect ratio of 0.5~0.7 compared to the radial sections where the aspect ratio is 0.6~0.9.
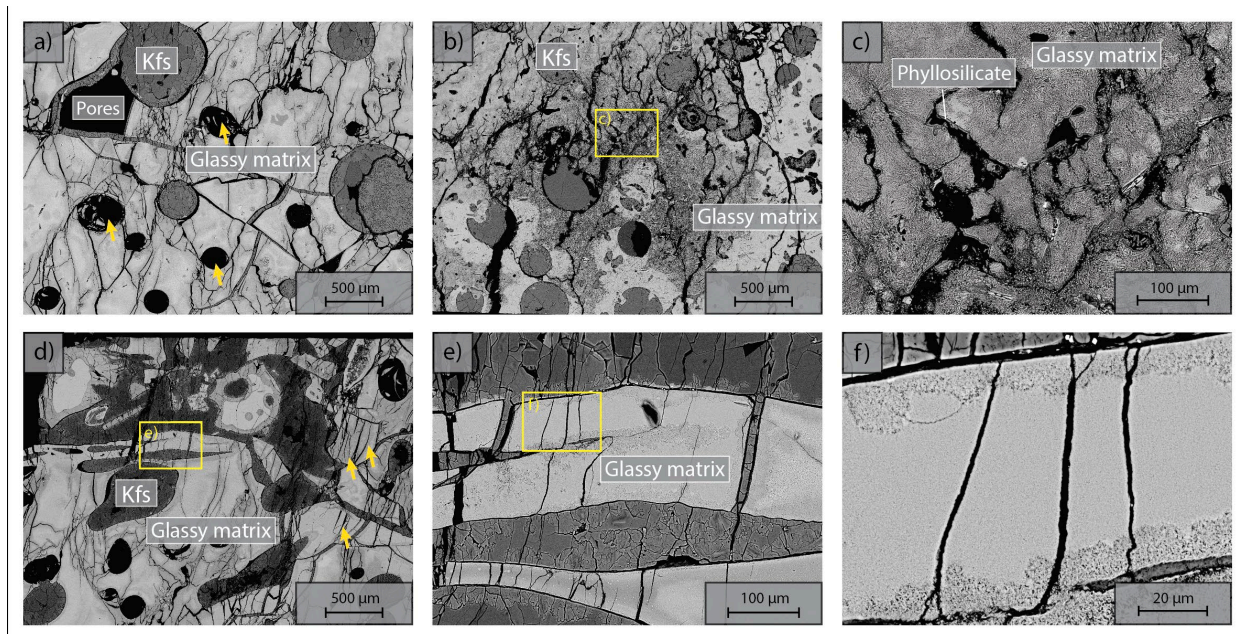
339
340 **Figure 12**. Microstructures of deformed sample from H_2O+CO_2 open experiment (OR3_B). Axial view, loading from
341 top and bottom. a) Pervasively fractured matrix, note the preferential N-S alignment of cracks indicating most cracks
342 are mode I. Note the collapse of void pores with cracks emanating (arrows). b) Crack pattern in altered glass matrix.
343 c) close up of b). Note the phyllosilicate coating on the crack wall. d - f) magnification cascade illustrating the crack
344 shape and morphology in the deformed sample.

345
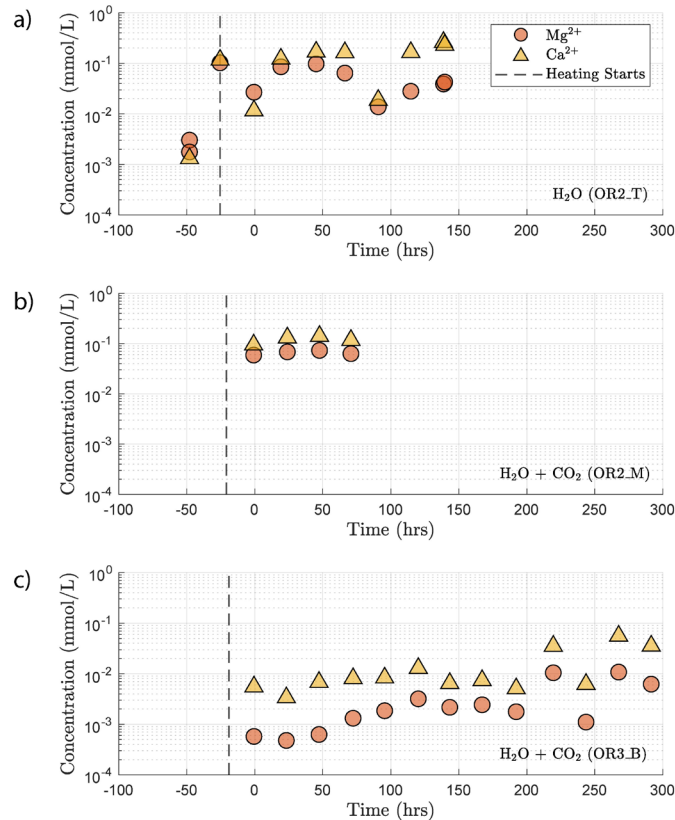
Figure 13. Concentration of Mg^{2+} and Ca^{2+} in the sampled fluid from a) H_2O, b) H_2O+CO_2 close and c) H_2O+CO_2
open experiments. Time 0 marks the start of the first creep stepping.

4. Discussion

4.1 Active Deformation Mechanisms

Acoustic emission, microstructure analysis and mechanical data confirm that the observed deformation is a brittle
process as is expected at the given P-T conditions. The strong similarity between the time evolution of cumulative AE
counts and strain (Figure 7 and 8) is consistent with observations from other creep deformation experiments using
cemented and uncemented porous rocks (e.g. Brzesowsky et al., 2014; Heap et al., 2009). These considerations suggest
that the creep deformation observed in this study is a result of a time-dependent brittle process such as subcritical
cracking, that can still generate AE activity (Chester et al., 2007; Chester et al., 2004).

Previous studies concluded that observable amount of brittle creep strain is unlikely to occur below 80% of ultimate
strength defined by the short-term, constant strain rate deformation experiments (Baud & Meredith, 1997; Heap et al.,
2009). However, all our strain measurements (strain gauges, LVDTs, axial ram displacement) show that, in this study,
creep did occur at stress levels of only ~11% of failure strength (and therefore even lower percentage of the ultimate
strength). Similar creep deformation with measurable strain at low stress level has been previously observed in shale
(e.g. Mighani et al., 2019). We also found that the strain rates measured during all creep steps could be fitted using
the same exponential law derived from strain rate measurements. Furthermore, the amount of creep strain accumulated

during phase I and phase II showed a consistent stress dependence across all stress conditions (Figure 4c and 4d). Therefore, our experiments demonstrated that there does not seem to exist a threshold below which no creep strain will be observed. The creep deformation was likely governed by the same mechanism across our tested stress conditions and the accumulated creep strain at a given time can be formulated as a function of stress.

Our AE statistics show that the b-values were higher for the fluid-saturated experiments than the dry experiment, indicating a higher proportion of low amplitude AEs (i.e., higher ratio of low-to-high amplitude events). This abundance of low amplitude events in fluid-saturated rock is a direct evidence that aqueous fluids promoted creep deformation in basalt. As argued in previous studies, growth of small cracks and low amplitude events are facilitated when stress corrosion is activated in the presence of aqueous fluids (Hatton et al., 1993). We also observed that the amplitude of the largest events increased with increasing stress. And this effect becomes more significant in the fluid saturated experiments (H_2O and H_2O+CO_2). This could be attributed to the increase in micro-crack nucleation, consequently maximizing the likelihood of an 'avalanche' of coalescing cracks, which, in turn, generates large amplitude events. Overall, as more and more energy is dissipated through micro-cracking and the associated low amplitude AEs, the macroscopic deformation becomes less dynamic, which is consistent with the increase in the Gutenberg-Richter b-value with increasing stress.

Post-mortem examination of the fluid-saturated samples demonstrated the presence of a complicated network of fractures within the sample and absence of a well-defined major shear fracture plane. The samples also exhibited distributed deformation features such as bulging, likely caused by the bulk formation of dilation cracks in addition to the cataclastic shear during the final failure. These microstructural observations further support the idea that deformation during creep is diffuse and distributed rather than localized (Hatton et al., 1993; Heap et al., 2009), consistent with nucleation-controlled crack growth since the nucleation sites are normally randomly distributed in the sample.

Microstructure analysis of the deformed samples demonstrates that the presence of fluid resulted in more abundant mode I cracks (Figure 11). Larger amount of cracks oriented parallel to the maximum principal stress were observed in the H_2O+CO_2 samples, implying dominant Mode I cracking, while the dry experiment showed less cracking, with the cracks aligned 20-30˚ to the maximum principal stress, thus pointing to mixed Mode I + Mode II cracking. This observation is consistent with previous studies on strain localization as they often proposed rock fracture models predicting that mode II cracking takes place during the localization stage of fracture development (Lockner et al., 1992; Reches and Lockner, 1994; Wong and Einstein, 2009). Among the present experiments, the samples subjected to creep deformation under H_2O+CO_2 conditions exhibited the largest amount of mode I cracks. The sample deformed under dry condition, despite having experienced similar differential stress and total accumulated strain, showed a lower amount of cracks. As stated in previous studies, mode II cracks often propagate at velocities close to the Rayleigh velocity, which increases the probability of occurrence of high amplitude events. On the other hand, mode I cracks have significantly lower rupture velocities and tend to produce low amplitude acoustic events (Broberg, 2006). Therefore, increased mode I cracking should lead to an increase in the proportion of low amplitude AEs, i.e. an increase in the Gutenberg-Richter b-value.

399 We infer that the difference in creep rate of the dry and fluid-saturated experiments is a result of fluid-assisted

400 subcritical crack growth. The fluid presence promotes stress corrosion, possibly related to hydrolytic weakening

401 (Atkinson, 1984), accelerates crack growth, activates more crack nucleation sites, and, consequently, leads to a

402 distributed array of small micro-cracks. In contrast, crack growth under dry conditions is concentrated on fewer and

403 larger cracks since activation of the nucleation sites is more difficult. Thus, it is easier to create localized deformation

404 under dry condition.

405 Previous studies also suggested that intergranular pressure solution (IPS) could play a significant role as a deformation

406 mechanism during creep (Liteanu et al., 2012; Zhang & Spiers, 2005; Zhang et al., 2010). The creep deformation by

407 IPS involves dissolution and the presence of a fluid phase might be expected to affect creep deformation, generating

408 additional strain accumulation apart from dilatant cracking. Importantly, because the driving process of IPS is not

409 producing abrupt stress drops, it is not expected to produce acoustic emissions. Although we did see difference in

410 creep strain between the dry and fluid-saturated experiments, it was likely caused by dynamic fracturing, as evidenced

411 by the volumetric strain and AE observations (Figure 5a and A1). We attribute the change in creep strain rate between

412 dry and fluid-saturated experiments to fluid-assisted subcritical crack growth. We posit that under our experimental

413 conditions, IPS was not a dominant creep mechanism, however more detailed microstructural observations are needed.

414 **4.2 Time and Stress Dependent Deformation**

415 Our experiments show that the time-dependent creep deformation was also strongly stress dependent. We observed

416 that the creep strain accumulated during phase I was exponentially dependent on stress (Figure 3c). Two exceptions

417 are noted in the dry experiment. Both showed high strain accumulation during phase I transient creep and followed a

418 sharp temporary stress drop during the creep step with a nominal differential stress of ~90 MPa (Figure 5). This

419 temporary stress drop was accompanied by a swarm of large amplitude AEs (Appendix Figure A2), implying that the

420 concurrent strong dilation was likely caused by local dynamic fracturing while the bulk of the sample remained mostly

421 intact and still capable of supporting the applied load.

422 We also observed an exponential relationship between stress and creep rate. Interestingly, the fluid-saturated

423 experiments yielded approximately equal stress sensitivities of the creep rates, $\dot{\varepsilon} \propto e^{0.02 \sim 0.03 \, \sigma}$, despite the variability

424 in their absolute strengths (Figure 3). The exponential stress dependence of strain rate in fluid-saturated experiments

425 is consistent with brittle creep being the dominant deformation mechanism. Indeed, the values of the fitting constant

426 (0.02~0.03) are comparable in order of magnitude to those reported in previous studies on other basaltic rocks (0.05

427 in Heap et al., 2011, from experiments using Etna Basalt). Since the creep rate was exponentially dependent on stress,

428 so should be the accumulated phase II creep strain. This inference is supported by our observation in Figure 4d.

429 Concerning the dry experiment, we attribute the slightly negative dependence of creep strain rate on stress (Figure 3e)

430 to statistical artefact owing to large data fluctuations as suggested by the low R^2 value of the exponential fitting

431 (Appendix Figure A6).

432 The fact that both cumulative phase I and phase II creep strains were exponentially dependent on stress (Figure 4c and

433 4d) implies a power-law relationship between the accumulated phase I and phase II creep strain. This power-law

434 relationship (i.e. the ratio between the logarithmic total phase I and logarithmic phase II creep strain), based on our

experimental observation, is independent of the stress level and even the presence or absence of fluids. This empirical relationship can be formulated as:

$$\frac{\log{(\varepsilon_t - \varepsilon_i)}}{\log{(\varepsilon_i)}} = \frac{\log{(\varepsilon_{ii})}}{\log{(\varepsilon_i)}} = cte. \qquad \text{(Eq. 8)}$$

where ε_t is the total strain accumulated at the end of an individual creep stage (~24 hrs), ε_i the creep strain accumulated during phase I, and ε_{ii} the strain accumulated during phase II (see Appendix Figure A5). This phenomenological power-law relationship is supported by our observation that the ratios in Equation 8 were indeed approximately constant ~0.8 (Figure 4a and 4b). This power-law relationship expressed in Equation 8 implies that the strain evolution with time can be predicted; some fundamental link between strain accommodated in phase I creep and strain rate in phase II creep exists.

4.3 Fluid Chemistry Evolution and Influence of Fluid Composition

The increase in concentration of both Mg^{2+} and Ca^{2+} occurring after heating in the H_2O and H_2O+CO_2 close experiment (Figure 13) indicates that the system was dominated by dissolution of Mg and Ca bearing minerals. In the case of the H_2O+CO_2 open experiment, we observed a much smaller increase in cation concentration implying that a significant amount of the released Mg^{2+} and Ca^{2+} cations reacted with the continuously supplied CO_2 in the semi-open setting to form carbonate precipitates. These cation concentration trends appeared strongly correlated with the permeability evolution and creep strength of the rocks. The experiment with H_2O+CO_2 open showed a larger post-heating permeability decrease than the experiments with H_2O and $H_2O + CO_2$ close and was stronger (Figures 3e and 6).The absolute creep rate was consistent for experiments with comparable fluid chemistry (H_2O and $H_2O + CO_2$ closed) and about a factor of 3 faster than in the experiment where precipitation was dominant ($H_2O + CO_2$ open) indicating that dissolution associated with fluid presence weakens the rock while precipitation reactions slightly strengthen the rock and partly compensate the effect of dissolution. This congruence of observations is a strong argument that precipitation occurred in the pore space of the CO_2 open experiment. However, we could not directly resolve evidence of precipitation within the resolution of our microstructural observations and this requires further study. Interestingly, the strain rate sensitivity to stress was similar in all fluid-saturated experiments (Figure 3), implying that creep rate sensitivity to stress was not significantly influenced by the fluid chemistry.

Our chemical data support the idea that carbonation of basalt is a kinetically favored reaction and are consistent with the fast rate of carbonation observed during the CarbFix field tests (Matter et al., 2016). We interpret the difference between the Mg^{2+} and Ca^{2+} concentrations measured in the H_2O+CO_2 open experiment and those in the H_2O and H_2O+CO_2 close experiments to be a result of the consumption of Mg^{2+} and Ca^{2+} in the formation of carbonate. This indicates that the supply of CO_2 is more sufficient in the H_2O+CO_2 open experiment andthe rate-limiting factor during carbonation under our experimental condition was the net supply of Mg^{2+} and Ca^{2+} cations, which is associated with dissolution.

4.4 Permeability & Porosity Evolution

Permeability was affected by both chemical and mechanical processes. The evolution of permeability during the experiments was generally consistent with previous observations of monotonic permeability decrease during

hydrostatic loading of samples of limestone, sandstone and Etna basalt (Brantut, 2015; Fortin et al., 2011; Zhu & Wong, 1997). Comparison of the dissolution dominated experiments (H_2O and H_2O+CO_2 close) and the precipitation dominated experiment (H_2O+CO_2 open) shows that the carbonation reaction reduced permeability in our experiment. In low differential stress conditions, the samples compacted and this compaction was accompanied by a further permeability decrease, which was likely related to the pore volume reduction expected during compressive deformation. Shortly before failure strength was reached, volumetric dilation became dominant and coincided with permeability increase. Our observations of the permeability evolution demonstrate that, although the permeability might decrease owing to compaction, formation and propagation of cracks can mitigate the permeability loss and even lead to an increase with further cracking. The effect of creep deformation on the long-term permeability evolution of reservoir rocks is therefore non-negligible. Increase in permeability, combined with other observations such as increasing volumetric strain and acoustic emissions, could potentially be used as a warning sign for impending failure during the long-term monitoring of reservoirs' integrity in GCS applications.

4.5 Effect of Sample Heterogeneity

As our samples are taken from drill cores collected at depth at the CarbFix carbon mineralization site, the heterogeneity is larger than in rocks typically used in rock mechanics experiments. The samples investigated in this study exhibit variations in their initial porosity (5-15%, see Table 1), failure strength (55-130 MPa) and Young's modulus (12-28 GPa). We observed a correlation between the failure strength and the elastic modulus of the samples where stiffer samples reach higher peak strengths, consistent with previous reports of an empirical relationship between the unconfined compressive strength and the elastic modulus of sedimentary rocks (see review in Chang et al., 2006). The peak strength however varied inversely with porosity; the dry sample (OR5), which has the highest initial porosity (15%), shows a higher failure strength (>105 MPa) and exhibits the lowest creep rate compared to the fluid-saturated experiments where porosity measurements were available (H_2O and H_2O+CO_2 close). Remarkably, the stress sensitivity of the creep strain rate shows consistency ($e^{0.02 - 0.03\,\sigma}$) in all the fluid saturated experiments (H_2O and H_2O+CO_2 open and close) in spite of these variations in porosity, stiffness and failure strength. Moreover, the creep rate at individual stress steps is consistent for experiments with comparable fluid chemistry (H_2O and $H_2O + CO_2$ closed) despite a variation in porosity by a factor of 2 in between the samples (Figure 3 and Table 1). These results are a strong argument for the operation of chemical processes that contribute to creep. While variations in porosity resulted in variation in peak strength, they did not seem to affect the absolute creep rates or the sensitivity of creep rate to stress.

5 Conclusions

Through the experimental study of long-term creep deformation of Iceland Basalt, we have demonstrated that:

- Transient creep occurred at stress levels as low as 11% of the failure strength.
- Presence of an aqueous pore fluid exerted first order control on the creep deformation of the basaltic rocks, while the fluid composition had only a secondary effect under our experimental conditions. At similar differential stress level, the creep rates in fluid-saturated experiments were much higher than the rates in the dry experiment.

- A close system tended to favor dissolution over precipitation during carbonation in our experimental setting, whereas precipitation played a more important role in an open system with continuous CO_2 supply.

- Larger amount of dilation was observed in fluid saturated experiments than in the dry experiment, as evidenced by both volumetric strain data and micro-structural observations.

- Larger low-to-high amplitude ratios of the AE events and higher AE rates were observed during the phase II creep of the fluid-saturated experiments than the dry experiment, indicating that aqueous fluids promoted stress corrosion processes.

- The mechanism governing the creep deformation was brittle, time- and stress-dependent, and could likely be identified as sub-critical dilatant cracking.

Overall, our results emphasize the non-negligible role that the creep deformation can potentially play in the long-term deformation of rocks even under low pressure and temperature conditions and calls for more attention to time-dependent processes such as sub-critical micro-cracking in GCS applications. Under our experimental conditions, the creep deformation and the associated fracture development were affected by the presence of aqueous fluids, implying that reactive fluids could potentially alter the fracture patterns and allow mineralization in a greater rock volume during GCS applications. Further detailed studies on the creep deformation under chemically active environment are required to better understand the long-term deformation of rocks in natural systems.

Acknowledgments, Samples, and Data

The authors benefited from discussions with Ben Holtzman, Yves Bernabé, Brian Evans, Bradford Hager and Brent Minchew. The author would like to thank Yves Bernabé for his copy editing of this paper. The author would also like to thank Edward Boyle and Richard Kayser for their help with the ICP-MS analysis. Funding by the MITei's Carbon Capture, Utilization and Storage Center, Scotiabank's Net Zero Research Fund and NSF funding for CORD laboratory technician support (EAR-1833478 and EAR-2054414) are gratefully acknowledged. The x-ray tomographic images were obtained at the Center for Nanoscale Systems (CNS), a member of the National Nanotechnology Coordinated Infrastructure Network (NNCI), which is supported by the National Science Foundation under NSF award no. 1541959. CNS is part of Harvard University. The cores used in this study were generously provided by Sandra Snæbjörnsdóttir and Kári Helgason. The authors declare no conflict of interest. The underlying data is available at http:// doi.org/10.5281/zenodo.4926587. The authors would like to thank Phillip Benson and the anonymous reviewer for their constructive and detailed reviews, and also thank editor David Healy and Federico Rossetti for the handling of this manuscript.

References

Alfredsson, H. A., Hardarson, B. S., Franzson, H. and Gislason, S. R.: CO2 sequestration in basaltic rock at the Hellisheidi site in SW Iceland: stratigraphy and chemical composition of the rocks at the injection site, Mineral. Mag., 72(1), 1–5, doi:10.1180/minmag.2008.072.1.1, 2008.

Alfredsson, H. A., Oelkers, E. H., Hardarsson, B. S., Franzson, H., Gunnlaugsson, E. and Gislason, S. R.: The geology and water chemistry of the Hellisheidi, SW-Iceland carbon storage site, Int. J. Greenh. Gas Control, 12, 399–418, doi:10.1016/j.ijggc.2012.11.019, 2013.

Anderson, O. L. and Grew, P. C.: Stress corrosion theory of crack propagation with applications to geophysics, Rev. Geophys., doi:10.1029/RG015i001p00077, 1977.

Aradóttir, E. S. P., Sonnenthal, E. L., Björnsson, G. and Jónsson, H.: Multidimensional reactive transport modeling of CO2 mineral sequestration in basalts at the Hellisheidi geothermal field, Iceland, Int. J. Greenh. Gas Control, 9, 24–40, doi:10.1016/J.IJGGC.2012.02.006, 2012.

Atkinson, B. K.: Subcritical crack growth in geological materials, J. Geophys. Res. Solid Earth, doi:10.1029/JB089iB06p04077, 1984.

Atkinson, B. K. and Meredith, P. G.: Fracture mechanics of rock- The Theory of Subcritical Crack Growth with

550   Applications to Minerals and Rocks, in Academic Press Geology Series., 1987.

551   Atkinson, G. M., Eaton, D. W. and Igonin, N.: Developments in understanding seismicity triggered by hydraulic
552   fracturing, Nat. Rev. Earth Environ., doi:10.1038/s43017-020-0049-7, 2020.

553   Baud, P. and Meredith, P. G.: Damage accumulation during triaxial creep of Darley Dale sandstone from pore
554   volumometry and acoustic emission, Int. J. rock Mech. Min. Sci. Geomech. Abstr., doi:10.1016/S1365-
555   1609(97)00060-9, 1997.

556   Baud, P., Zhu, W. and Wong, T.: Failure mode and weakening effect of water on sandstone, J. Geophys. Res. Solid
557   Earth, doi:10.1029/2000jb900087, 2000.

558   Brace, W. F., Paulding, B. W. and Scholz, C. H.: Dilatancy in the fracture of crystalline rocks, J. Geophys. Res.,
559   doi:10.1029/jz071i016p03939, 1966.

560   Brantut, N.: Time-dependent recovery of microcrack damage and seismic wave speeds in deformed limestone, J.
561   Geophys. Res. Solid Earth, 120(12), 8088–8109, doi:10.1002/2015JB012324, 2015.

562   Brantut, N., Baud, P., Heap, M. J. and Meredith, P. G.: Micromechanics of brittle creep in rocks, J. Geophys. Res.
563   Solid Earth, doi:10.1029/2012JB009299, 2012.

564   Brantut, N., Heap, M. J., Meredith, P. G. and Baud, P.: Time-dependent cracking and brittle creep in crustal rocks: A
565   review, J. Struct. Geol., 52(1), 17–43, doi:10.1016/j.jsg.2013.03.007, 2013.

566   Broberg, K. B.: Differences Between Mode I and Mode II Crack Propagation, Pure Appl. Geophys., 163(9), 1867–
567   1879, doi:10.1007/s00024-006-0101-7, 2006.

568   Broecker, W. S.: Climatic change: Are we on the brink of a pronounced global warming?, Science (80-.).,
569   doi:10.1126/science.189.4201.460, 1975.

570   Brzesowsky, R. H., Hangx, S. J. T., Brantut, N. and Spiers, C. J.: Compaction creep of sands due to time-dependent
571   grain failure: Effects of chemical environment, applied stress, and grain size, J. Geophys. Res. Solid Earth, 119(10),
572   7521–7541, doi:10.1002/2014JB011277, 2014.

573   Callow, B., Falcon-Suarez, I., Ahmed, S. and Matter, J. M.: Assessing the carbon sequestration potential of basalt
574   using X-ray micro-CT and rock mechanics, Int. J. Greenh. Gas Control, 70(December 2017), 146–156,
575   doi:10.1016/j.ijggc.2017.12.008, 2018.

576   Chang, C., Zoback, M. D. and Khaksar, A.: Empirical relations between rock strength and physical properties in
577   sedimentary rocks, J. Pet. Sci. Eng., doi:10.1016/j.petrol.2006.01.003, 2006.

578   Charles, R. J. and Hillig, W. B.: The Kinetics of Glass Failure by Stress Corrosion, in Symposium on Mechanical
579   Strength of Glass and Ways of Improving It., 1962.

580   Chester, F. M., Chester, J. S., Kronenberg, A. K. and Hajash, A.: Subcritical creep compaction of quartz sand at
581   diagenetic conditions: Effects of water and grain size, J. Geophys. Res., 112(B6), B06203,
582   doi:10.1029/2006JB004317, 2007.

583   Chester, J. ., Lenz, S. ., Chester, F. . and Lang, R. .: Mechanisms of compaction of quartz sand at diagenetic
584   conditions, Earth Planet. Sci. Lett., 220(3–4), 435–451, doi:10.1016/S0012-821X(04)00054-8, 2004.

585   Dunkel, K. G., Austrheim, H., Renard, F., Cordonnier, B. and Jamtveit, B.: Localized slip controlled by dehydration
586   embrittlement of partly serpentinized dunites, Leka Ophiolite Complex, Norway, Earth Planet. Sci. Lett., 463, 277–
587   285, doi:10.1016/j.epsl.2017.01.047, 2017.

588   Dunning, J. D. and Miller, M. E.: Effects of pore fluid chemistry on stable sliding of Berea sandstone, Pure Appl.
589   Geophys. PAGEOPH, 122(2–4), 447–462, doi:10.1007/BF00874611, 1985.

590   Fortin, J., Stanchits, S., Vinciguerra, S. and Guéguen, Y.: Influence of thermal and mechanical cracks on
591   permeability and elastic wave velocities in a basalt from Mt. Etna volcano subjected to elevated pressure,
592   Tectonophysics, 503(1–2), 60–74, doi:10.1016/j.tecto.2010.09.028, 2011.

593   Ghaffari, H. O. and Pec, M.: An ultrasound probe array for a high-pressure, high-temperature solid medium
594   deformation apparatus, Rev. Sci. Instrum., 91(8), 085117, doi:10.1063/5.0004035, 2020.

595 Ghaffari, H. O., Mok, U. and Pec, M.: On calibration of piezoelectric sensors with laser doppler vibrometer, J.
596 Acoust. Soc. Am., 150(4), 2503, doi:10.1121/10.0006445, 2021.

597 Gislason, S. R. and Hans, P. E.: Meteoric water-basalt interactions. I: A laboratory study, Geochim. Cosmochim.
598 Acta, doi:10.1016/0016-7037(87)90161-X, 1987.

599 Gislason, S. R. and Oelkers, E. H.: Carbon Storage in Basalt, Science (80-.)., 344(6182), 373–374,
600 doi:10.1126/science.1250828, 2014.

601 Gislason, S. R., Wolff-Boenisch, D., Stefansson, A., Oelkers, E. H., Gunnlaugsson, E., Sigurdardottir, H., Sigfusson,
602 B., Broecker, W. S., Matter, J. M. and Stute, M.: Mineral sequestration of carbon dioxide in basalt: A pre-injection
603 overview of the CarbFix project, Int. J. Greenh. Gas Control, 4(3), 537–545, doi:10.1016/j.ijggc.2009.11.013, 2010.

604 Goff, F. and Lackner, K. S.: Carbon dioxide sequestering using ultramafic rocks, Environ. Geosci., 5(3), 89 LP –
605 101, doi:10.1046/j.1526-0984.1998.0a8014.x, 1998.

606 Guglielmi, Y., Cappa, F., Avouac, J. P., Henry, P. and Elsworth, D.: Seismicity triggered by fluid injection-induced
607 aseismic slip, Science (80-.)., doi:10.1126/science.aab0476, 2015.

608 Hangx, S. J. T. and Spiers, C. J.: Reaction of plagioclase feldspars with CO2 under hydrothermal conditions, Chem.
609 Geol., doi:10.1016/j.chemgeo.2008.12.005, 2009.

610 Hansen, L. D., Dipple, G. M., Gordon, T. M. and Kellett, D. A.: CARBONATED SERPENTINITE
611 (LISTWANITE) AT ATLIN, BRITISH COLUMBIA: A GEOLOGICAL ANALOGUE TO CARBON DIOXIDE
612 SEQUESTRATION, Can. Mineral., 43(1), 225–239, doi:10.2113/gscanmin.43.1.225, 2005.

613 Hatton, C. G., Main, I. G. and Meredith, P. G.: A comparison of seismic and structural measurements of scaling
614 exponents during tensile subcritical crack growth, J. Struct. Geol., doi:10.1016/0191-8141(93)90008-X, 1993.

615 Heap, M. J., Baud, P., Meredith, P. G., Bell, A. F. and Main, I. G.: Time-dependent brittle creep in darley dale
616 sandstone, J. Geophys. Res. Solid Earth, 114(7), 1–22, doi:10.1029/2008JB006212, 2009.

617 Heap, M. J., Baud, P., Meredith, P. G., Vinciguerra, S., Bell, A. F. and Main, I. G.: Brittle creep in basalt and its
618 application to time-dependent volcano deformation, Earth Planet. Sci. Lett., 307(1–2), 71–82,
619 doi:10.1016/j.epsl.2011.04.035, 2011.

620 Heard, H. C.: Chapter 7: Transition from Brittle Fracture to Ductile Flow in Solenhofen Limestone as a Function of
621 Temperature, Confining Pressure, and Interstitial Fluid Pressure, Geol. Soc. Am. Mem., doi:10.1130/MEM79-p193,
622 1960.

623 Heilbronner, R. and Barrett, S.: Image Analysis in Earth Sciences, Springer Berlin Heidelberg, Berlin, Heidelberg.,
624 2014.

625 Helmons, R. L. J., Miedema, S. A. and van Rhee, C.: Simulating hydro mechanical effects in rock deformation by
626 combination of the discrete element method and the smoothed particle method, Int. J. Rock Mech. Min. Sci.,
627 doi:10.1016/j.ijrmms.2016.04.018, 2016.

628 Hillig, W. B.: The C-H delayed failure mechanism revisited, Int. J. Fract., doi:10.1007/s10704-006-0025-3, 2006.

629 Iyer, K., Jamtveit, B., Mathiesen, J., Malthe-Sørenssen, A. and Feder, J.: Reaction-assisted hierarchical fracturing
630 during serpentinization, Earth Planet. Sci. Lett., 267(3–4), 503–516, doi:10.1016/j.epsl.2007.11.060, 2008.

631 Jamtveit, B., Putnis, C. V. and Malthe-Sørenssen, A.: Reaction induced fracturing during replacement processes,
632 Contrib. to Mineral. Petrol., 157(1), 127–133, doi:10.1007/s00410-008-0324-y, 2009.

633 Kanakiya, S., Adam, L., Esteban, L., Rowe, M. C. and Shane, P.: Dissolution and secondary mineral precipitation in
634 basalts due to reactions with carbonic acid, J. Geophys. Res. Solid Earth, doi:10.1002/2017JB014019, 2017.

635 Kelemen, P. B. and Hirth, G.: Reaction-driven cracking during retrograde metamorphism: Olivine hydration and
636 carbonation, Earth Planet. Sci. Lett., 345–348, 81–89, doi:10.1016/j.epsl.2012.06.018, 2012.

637 Kelemen, P. B. and Matter, J. M.: In situ carbonation of peridotite for CO2 storage, Proc. Natl. Acad. Sci. U. S. A.,
638 105(45), 17295–17300, doi:10.1073/pnas.0805794105, 2008.

639 Kelemen, P. B., Savage, H. M. and Hirth, G.: Reaction-Driven Cracking During Mineral Hydration, Carbonation

640 and Oxidation, in Poromechanics V, vol. c, pp. 823–826, American Society of Civil Engineers, Reston, VA., 2013.

641 Kranz, R. L., Harris, W. J. and Carter, N. L.: Static fatigue of granite at 200°C, Geophys. Res. Lett.,
642 doi:10.1029/GL009i001p00001, 1982.

643 Lackner, K. S., Wendt, C. H., Butt, D. P., Joyce, E. L. and Sharp, D. H.: Carbon dioxide disposal in carbonate
644 minerals, Energy, 20(11), 1153–1170, doi:10.1016/0360-5442(95)00071-N, 1995.

645 Lambart, S., Savage, H. M., Robinson, B. G. and Kelemen, P. B.: Experimental Investigation of the Pressure of
646 Crystallization of Ca(OH) 2 : Implications for the Reactive Cracking Process, Geochemistry, Geophys. Geosystems,
647 doi:10.1029/2018GC007609, 2018.

648 Larsson, D., Grönvold, K., Oskarsson, N. and Gunnlaugsson, E.: Hydrothermal alteration of plagioclase and growth
649 of secondary feldspar in the Hengill Volcanic Centre, SW Iceland, J. Volcanol. Geotherm. Res., 114(3–4), 275–290,
650 doi:10.1016/S0377-0273(01)00267-0, 2002.

651 Lisabeth, H. P., Zhu, W., Xing, T. and De Andrade, V.: Dissolution-Assisted Pattern Formation During Olivine
652 Carbonation, Geophys. Res. Lett., 44(19), 9622–9631, doi:10.1002/2017GL074393, 2017.

653 Liteanu, E., Niemeijer, A. R., Spiers, C. J., Peach, C. J. and De Bresser, J. H. P.: The effect of CO2 on creep of wet
654 calcite aggregates, J. Geophys. Res. Solid Earth, 117(3), doi:10.1029/2011JB008789, 2012.

655 Lockner, D. A.: The role of acoustic emission in the study of rock fracture, Int. J. Rock Mech. Min. Sci.,
656 doi:10.1016/0148-9062(93)90041-B, 1993.

657 Lockner, D. A., Byerlee, J. D., Kuksenko, V., Ponomarev, A. and Sidorin, A.: Observations of Quasistatic Fault
658 Growth from Acoustic Emissions, Int. Geophys., doi:10.1016/S0074-6142(08)62813-2, 1992.

659 Macdonald, A. H. and Fyfe, W. S.: Rate of serpentinization in seafloor environments, Tectonophysics, 116(1–2),
660 123–135, doi:10.1016/0040-1951(85)90225-2, 1985.

661 Mani, D., Nirmal Charan, S. and Kumar, B.: Assessment of carbon dioxide sequestration potential of ultramafic
662 rocks in the greenstone belts of southern India, Curr. Sci., 94(1), 53–60, 2008.

663 Matter, J. M. and Kelemen, P. B.: Permanent storage of carbon dioxide in geological reservoirs by mineral
664 carbonation, Nat. Geosci., 2(12), 837–841, doi:10.1038/ngeo683, 2009.

665 Matter, J. M., Takahashi, T. and Goldberg, D. S.: Experimental evaluation of in situ CO2-water-rock reactions
666 during CO2 injection in basaltic rocks: Implications for geological CO2 sequestration, Geochemistry, Geophys.
667 Geosystems, doi:10.1029/2006GC001427, 2007.

668 Matter, J. M., Stute, M., Snaebjornsdottir, S. O., Oelkers, E. H., Gislason, S. R., Aradottir, E. S., Sigfusson, B.,
669 Gunnarsson, I., Sigurdardottir, H., Gunnlaugsson, E., Axelsson, G., Alfredsson, H. A., Wolff-Boenisch, D., Mesfin,
670 K., Taya, D. F. d. l. R., Hall, J., Dideriksen, K. and Broecker, W. S.: Rapid carbon mineralization for permanent
671 disposal of anthropogenic carbon dioxide emissions, Science (80-.)., 352(6291), 1312–1314,
672 doi:10.1126/science.aad8132, 2016.

673 McGrail, B. P., Schaef, H. T., Ho, A. M., Chien, Y. J., Dooley, J. J. and Davidson, C. L.: Potential for carbon
674 dioxide sequestration in flood basalts, J. Geophys. Res. Solid Earth, doi:10.1029/2005JB004169, 2006.

675 McGrail, B. P., Spane, F. A. A., Sullivan, E. C., Bacon, D. H. and Hund, G.: The Wallula basalt sequestration pilot
676 project, Energy Procedia, 4, 5653–5660, doi:10.1016/j.egypro.2011.02.557, 2011.

677 McGrail, B. P., Schaef, H. T., Spane, F. A., Horner, J. A., Owen, A. T., Cliff, J. B., Qafoku, O., Thompson, C. J. and
678 Sullivan, E. C.: Wallula Basalt Pilot Demonstration Project: Post-injection Results and Conclusions, Energy
679 Procedia, 114, 5783–5790, doi:10.1016/j.egypro.2017.03.1716, 2017.

680 Meredith, P. G. and Atkinson, B. K.: Stress corrosion and acoustic emission during tensile crack propagation in
681 Whin Sill dolerite and other basic rocks, Geophys. J. R. Astron. Soc., 75(1), 1–21, doi:10.1111/j.1365-
682 246X.1983.tb01911.x, 1983.

683 Michalske, T. A. and Freiman, S. W.: A Molecular Mechanism for Stress Corrosion in Vitreous Silica, J. Am.
684 Ceram. Soc., doi:10.1111/j.1151-2916.1983.tb15715.x, 1983.

685 Mighani, S., Bernabé, Y., Boulenouar, A., Mok, U. and Evans, B.: Creep Deformation in Vaca Muerta Shale From

686   Nanoindentation to Triaxial Experiments, J. Geophys. Res. Solid Earth, doi:10.1029/2019JB017524, 2019.

687   Nara, Y., Yamanaka, H., Oe, Y. and Kaneko, K.: Influence of temperature and water on subcritical crack growth
688   parameters and long-term strength for igneous rocks, Geophys. J. Int., doi:10.1093/gji/ggs116, 2013.

689   National Academies of Sciences, Engineering, and M.: Negative Emissions Technologies and Reliable
690   Sequestration: A Research Agenda, National Academies Press, Washington, D.C., 2019.

691   Oelkers, E. H., Gislason, S. R. and Matter, J. M.: Mineral carbonation of CO2, Elements, 4(5), 333–337,
692   doi:10.2113/gselements.4.5.333, 2008.

693   Orowan, E.: The fatigue of glass under stress, Nature, 154(3906), 341–343, doi:10.1038/154341a0, 1944.

694   Panozzo, R. É.: Two-dimensional strain from the orientation of lines in a plane, J. Struct. Geol., doi:10.1016/0191-
695   8141(84)90098-1, 1984.

696   Reber, J. E. and Pec, M.: Comparison of brittle- and viscous creep in quartzites: Implications for semi-brittle flow of
697   rocks, J. Struct. Geol., doi:10.1016/j.jsg.2018.05.022, 2018.

698   Reches, Z. and Lockner, D. A.: Nucleation and growth of faults in brittle rocks, J. Geophys. Res. Solid Earth,
699   doi:10.1029/94jb00115, 1994.

700   Renard, F., Gundersen, E., Hellmann, R., Collombet, M. and Le Guen, Y.: Numerical modeling of the effect of
701   carbon dioxide sequestration on the rate of pressure solution creep in limestone: Preliminary results, Oil Gas Sci.
702   Technol., doi:10.2516/ogst:2005023, 2005.

703   Renard, F., Kandula, N., McBeck, J. and Cordonnier, B.: Creep Burst Coincident With Faulting in Marble Observed
704   in 4-D Synchrotron X-Ray Imaging Triaxial Compression Experiments, J. Geophys. Res. Solid Earth,
705   doi:10.1029/2020JB020354, 2020.

706   Rice, J. R.: Thermodynamics of the quasi-static growth of Griffith cracks, J. Mech. Phys. Solids, doi:10.1016/0022-
707   5096(78)90014-5, 1978.

708   Robertson, E. C.: Creep of Solenhofen Limestone Under Moderate Hydrostatic Pressure, pp. 227–244., 1960.

709   Robertson, E. C.: Viscoelasticity of rocks, State Stress Earth's Crust, 181–233, 1964.

710   Rudge, J. F., Kelemen, P. B. and Spiegelman, M.: A simple model of reaction-induced cracking applied to
711   serpentinization and carbonation of peridotite, Earth Planet. Sci. Lett., 291(1–4), 215–227,
712   doi:10.1016/j.epsl.2010.01.016, 2010.

713   Rutter, E. H.: The influence of interstitial water on the rheological behaviour of calcite rocks, Tectonophysics,
714   doi:10.1016/0040-1951(72)90003-0, 1972.

715   Rutter, E. H. and Hackston, A.: On the effective stress law for rock-on-rock frictional sliding, and fault slip triggered
716   by means of fluid injection, Philos. Trans. R. Soc. A Math. Phys. Eng. Sci., 375(2103), doi:10.1098/rsta.2016.0001,
717   2017.

718   Scholz, C. H.: Mechanism of creep in brittle rock, J. Geophys. Res., doi:10.1029/JB073i010p03295, 1968.

719   Scholz, C. H.: Static fatigue of quartz, J. Geophys. Res., doi:10.1029/JB077i011p02104, 1972.

720   Seifritz, W.: CO2 disposal by means of silicates, Nature, 345(6275), 486–486, doi:10.1038/345486b0, 1990.

721   Skarbek, R. M., Savage, H. M., Kelemen, P. B. and Yancopoulos, D.: Competition Between Crystallization-Induced
722   Expansion and Creep Compaction During Gypsum Formation, and Implications for Serpentinization, J. Geophys.
723   Res. Solid Earth, 123(7), 5372–5393, doi:10.1029/2017JB015369, 2018.

724   Snæbjörnsdóttir, S. Ó. and Gislason, S. R.: CO2 Storage Potential of Basaltic Rocks Offshore Iceland, Energy
725   Procedia, 86, 371–380, doi:10.1016/j.egypro.2016.01.038, 2016.

726   Snæbjörnsdóttir, S. Ó., Gislason, S. R., Galeczka, I. M. and Oelkers, E. H.: Reaction path modelling of in-situ
727   mineralisation of CO2 at the CarbFix site at Hellisheidi, SW-Iceland, Geochim. Cosmochim. Acta, 220, 348–366,
728   doi:10.1016/j.gca.2017.09.053, 2018.

729   Snæbjörnsdóttir, S. Ó., Sigfússon, B., Marieni, C., Goldberg, D., Gislason, S. R. and Oelkers, E. H.: Carbon dioxide

730   storage through mineral carbonation, Nat. Rev. Earth Environ., doi:10.1038/s43017-019-0011-8, 2020.

731   Terzaghi, K.: Theoretical soil mechanics, Chapman And Hall, Limited., London., 1943.

732   Tutolo, B. M., Awolayo, A. and Brown, C.: Alkalinity Generation Constraints on Basalt Carbonation for Carbon
733   Dioxide Removal at the Gigaton-per-Year Scale, Environ. Sci. Technol., 55(17), 11906–11915,
734   doi:10.1021/ACS.EST.1C02733/SUPPL_FILE/ES1C02733_SI_002.XLSX, 2021.

735   Vajdova, V., Baud, P., Wu, L. and Wong, T. fong: Micromechanics of inelastic compaction in two allochemical
736   limestones, J. Struct. Geol., doi:10.1016/j.jsg.2012.07.006, 2012.

737   Wong, L. N. Y. and Einstein, H. H.: Systematic evaluation of cracking behavior in specimens containing single
738   flaws under uniaxial compression, Int. J. Rock Mech. Min. Sci., doi:10.1016/j.ijrmms.2008.03.006, 2009.

739   Xing, T., Zhu, W., Fusseis, F. and Lisabeth, H. P.: Generating porosity during olivine carbonation via dissolution
740   channels and expansion cracks, Solid Earth, 9(4), 879–896, doi:10.5194/se-9-879-2018, 2018.

741   Zakharova, N. V., Goldberg, D. S., Sullivan, E. C., Herron, M. M. and Grau, J. A.: Petrophysical and geochemical
742   properties of Columbia River flood basalt: Implications for carbon sequestration, Geochemistry, Geophys.
743   Geosystems, 13(11), 1–22, doi:10.1029/2012GC004305, 2012.

744   Zhang, X. and Spiers, C. J.: Compaction of granular calcite by pressure solution at room temperature and effects of
745   pore fluid chemistry, Int. J. Rock Mech. Min. Sci., doi:10.1016/j.ijrmms.2005.05.017, 2005.

746   Zhang, X., Spiers, C. J. and Peach, C. J.: Compaction creep of wet granular calcite by pressure solution at 28°C to
747   150°C, J. Geophys. Res. Solid Earth, doi:10.1029/2008JB005853, 2010.

748   Zhang, Z. L., Xu, W. Y., Wang, W. and Wang, R. B.: Triaxial creep tests of rock from the compressive zone of dam
749   foundation in Xiangjiaba Hydropower Station, Int. J. Rock Mech. Min. Sci., doi:10.1016/j.ijrmms.2012.01.003,
750   2012.

751   Zhu, W. and Wong, T.: The transition from brittle faulting to cataclastic flow: Permeability evolution, J. Geophys.
752   Res. Solid Earth, doi:10.1029/96jb03282, 1997.

753   Zhu, W., Baud, P. and Wong, T. F.: Micromechanics of cataclastic pore collapse in limestone, J. Geophys. Res.
754   Solid Earth, doi:10.1029/2009JB006610, 2010.

755   Zhu, W., Fusseis, F., Lisabeth, H. P., Xing, T., Xiao, X., De Andrade, V. and Karato, S.: Experimental evidence of
756   reaction-induced fracturing during olivine carbonation, Geophys. Res. Lett., 43(18), 9535–9543,
757   doi:10.1002/2016GL070834, 2016.

758

Appendices

760   **A.1 Sample Composition**
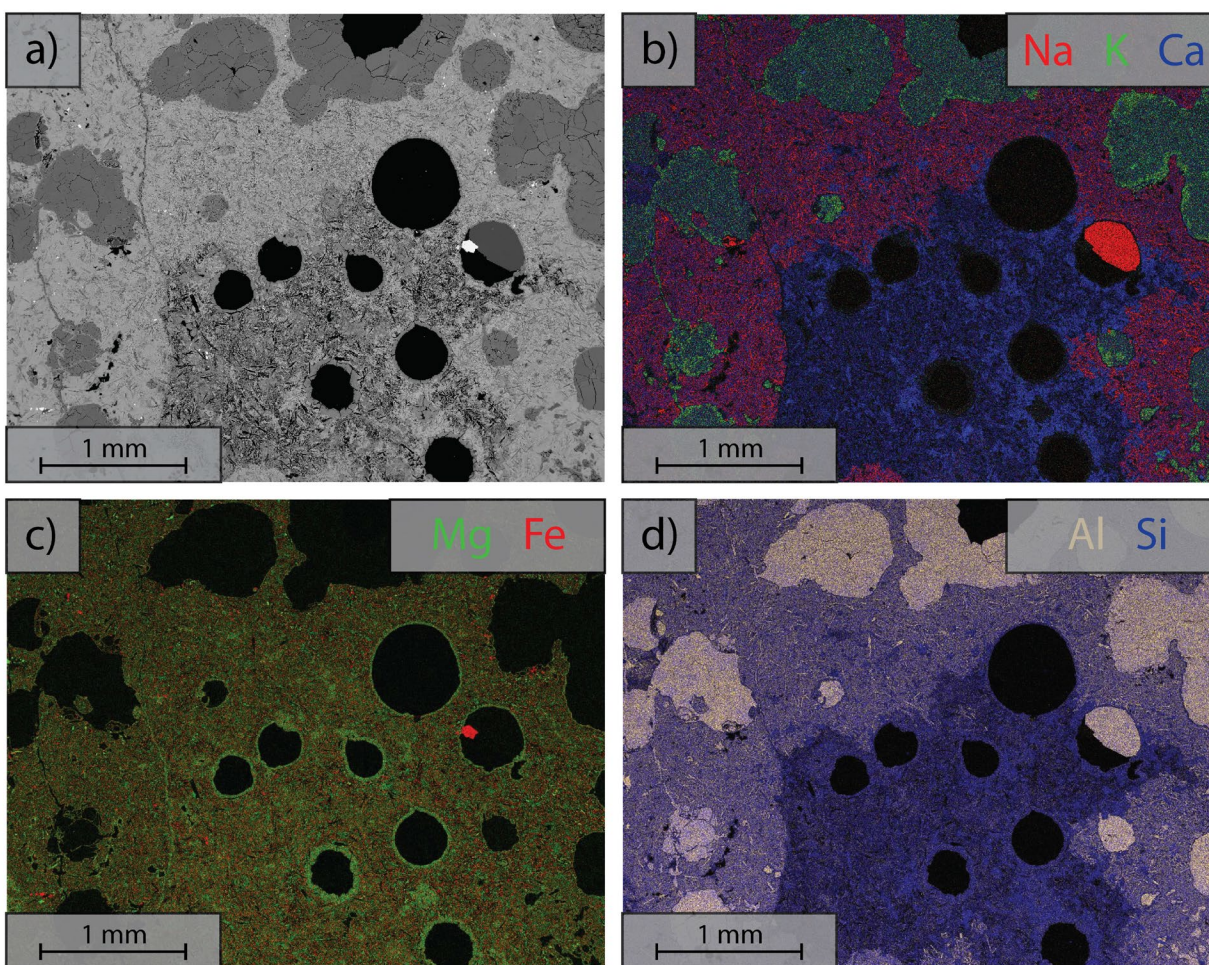
761
762   **Figure A1** Energy Dispersive Spectroscopy (EDS) analysis of the area marked in Figure 1; Color composite images
763   are made by combining RGB channel where the individual channels contain element concentration. a) Backscattered
764   electron (BSE) images of the starting material; b) Elemental composition of Na K and Ca; c) Elemental composition
765   of Mg and Fe; d) Elemental composition of Al and Si.

 A.2 Experimental Procedures

767
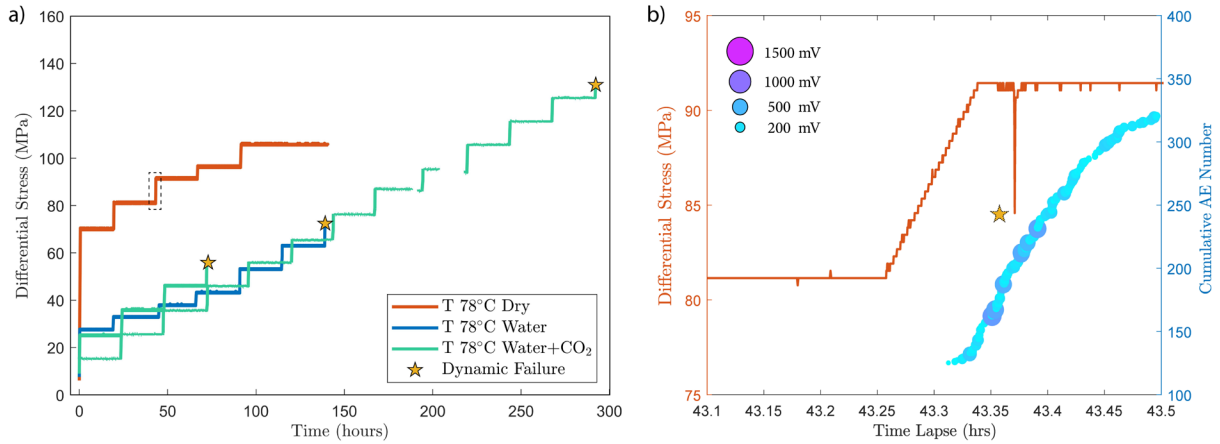
Figure A2 a) Differential stress vs time plot of experiments conducted at temperature of 78˚C. The dry experiment
(red) was ceased before dynamic failure occurred in the sample. b) A temporary stress drop was observed (highlighted
by the dashed rectangle in a)) during the primary creep of the dry experiment at creep stress of ~90 MPa accompanied
by the occurrence of high amplitude AEs.

A.2 Phase I to Phase II Transient Creep Transition

Selection of the phase II transient creep from the mechanical data is based on the calculated strain rate using first
derivative of the strain curve vs. time at different stress levels (Figure A2). The plot of strain rate vs strain further
supported that the strain rate evolution slows down during the identified phase II creep.

776
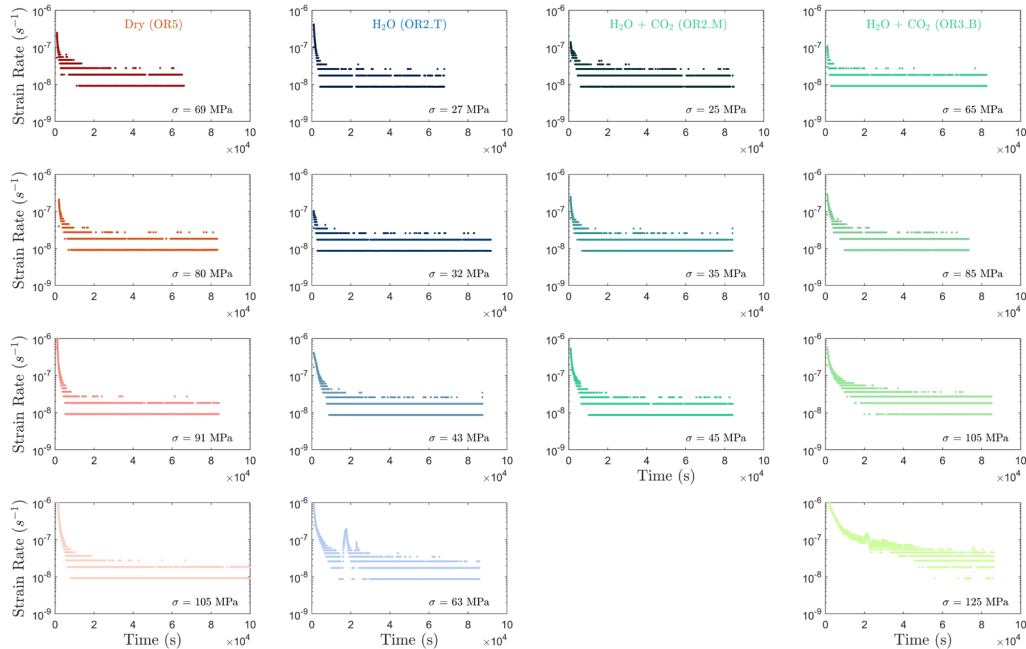
Figure A3 Strain rate evolution calculated from the first derivative of the strain vs. time data. It can be observed that
the strain rates generally become constant 10,000 s ($\approx$2.8 h) after the load stepping in most steps.
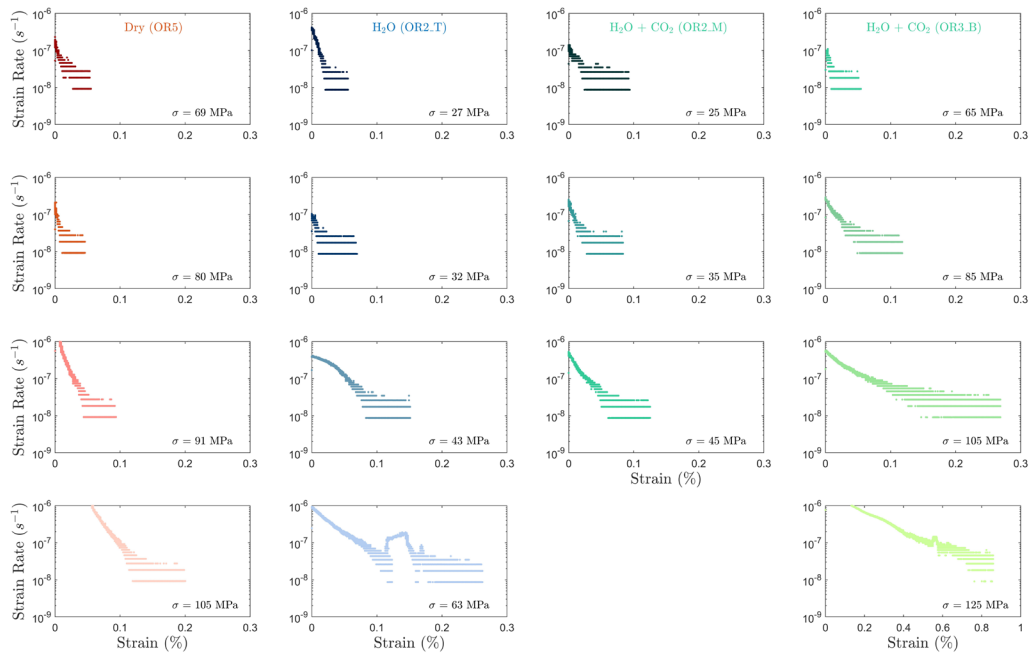
779

780 **Figure A4** Plot of strain rate evolution vs. strain.

781 To consistently analyze the transition between phase I and phase II of the transient creep, we fit the evolution of phase
782 I creep strain over time using a power-law function and the phase II creep strain as a linear function (Figure A3 a).
783 The measured strain data point that is the closest to the intersection of the two fitting functions is selected as the
784 inflection point, i.e., the transition from phase I to phase II transient creep deformation. Figure A3 b and c shows the
785 logarithmic and power-law fitting methods used for the time evolution of creep strain (ε). With the 24 hrs observation
786 window of our experiment.
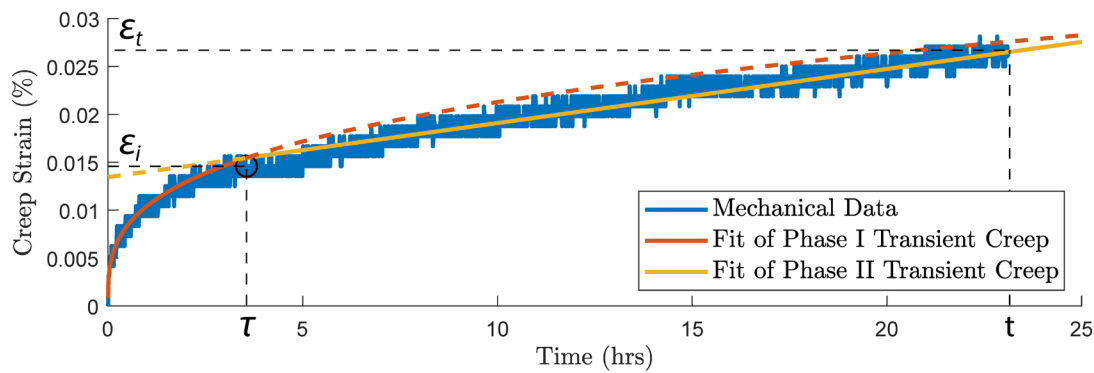
787

788 **Figure A5** illustration of the method used to pick up the transition (circle) from phase I to phase II transient creep
789 deformation. a) Two phase model for the time evolution of creep strain. The transition (circle) from phase I to phase
790 II creep deformation is selected based on the intersection of the power-law fit function of phase I creep (red) and linear
791 fit function of the phase II creep (yellow).

A.3 Creep Strain/Stress Models

The strain rate during phase II creep deformation is generally described using the power law form (e.g. Atkinson, 1984; Meredith and Atkinson, 1983):

$$d\varepsilon/dt = A\sigma^n \qquad \text{(Eq. A1)}$$

or the exponential form (e.g. Charles and Hillig, 1962):

$$d\varepsilon/dt = Be^{\eta\sigma} \qquad \text{(Eq. A2)}$$

where ε is the creep strain and σ is the differential stress. A, B, n and η are constants. Both models have described our laboratory data well. The exponential model seems to be slightly better than the power law model when comparing the R^2 factors.
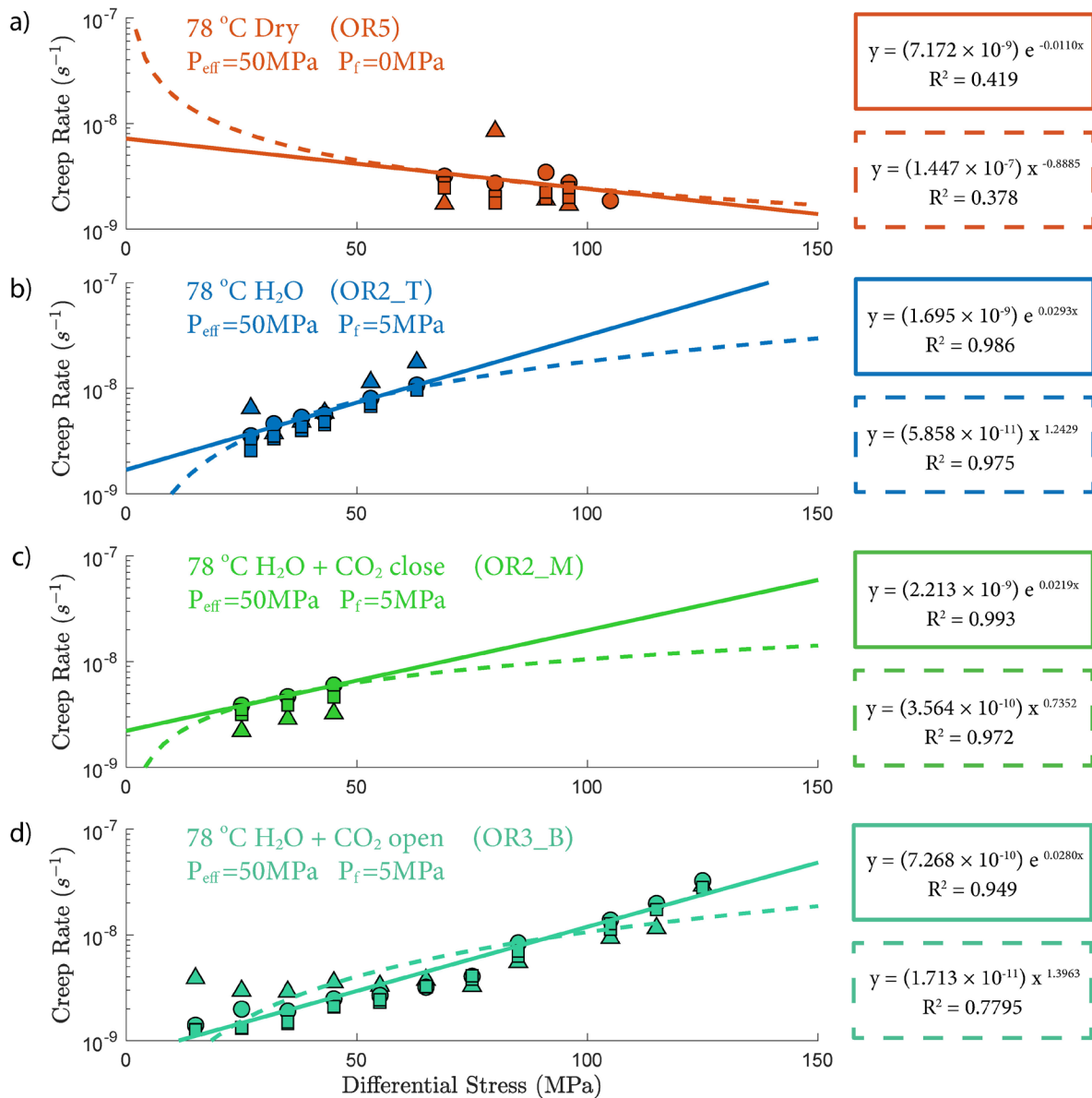
Figure A6 Power-law (dash line) and exponential (solid line) fit of creep rate/stress relationship. The strain rates are calculated from strain measurement from main ram displacement (circle), strain gauge (triangle) and LVDTs (square).

804 **A.4 Gutenberg-Richter b-value**

805 Figure A6 shows the fitting of the Gutenberg-Richter b-value from different experiments at various stress levels.
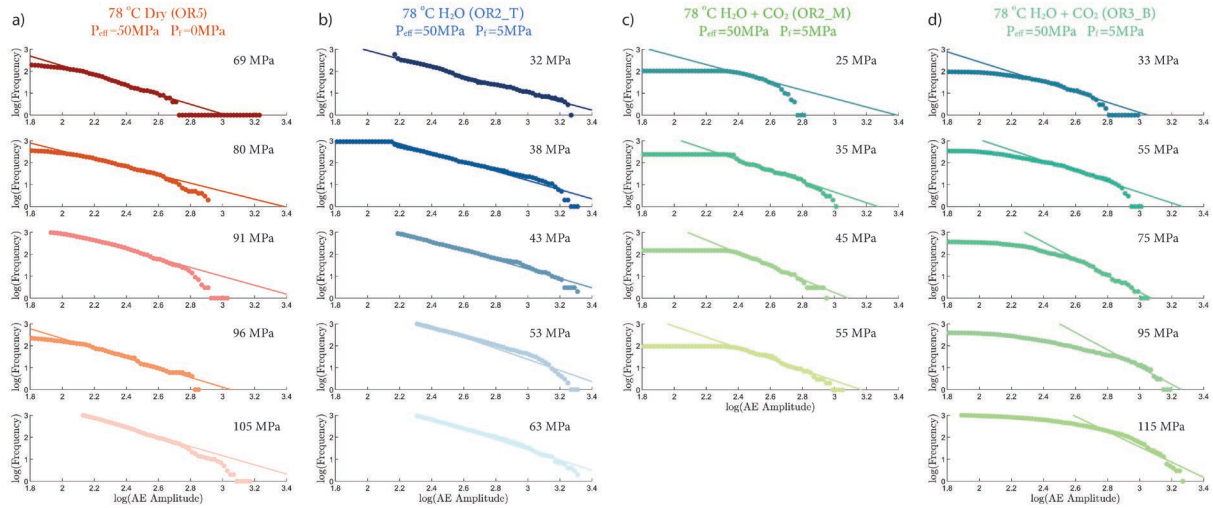
806
807 **Figure A7** Statistics of AE amplitudes for Gutenberg-Richter b-value calculation from a) dry, b) H_2O c) H_2O+CO_2
808 close and d) H_2O+CO_2 open experiments.

809 **A.5 Samples after Deformation**
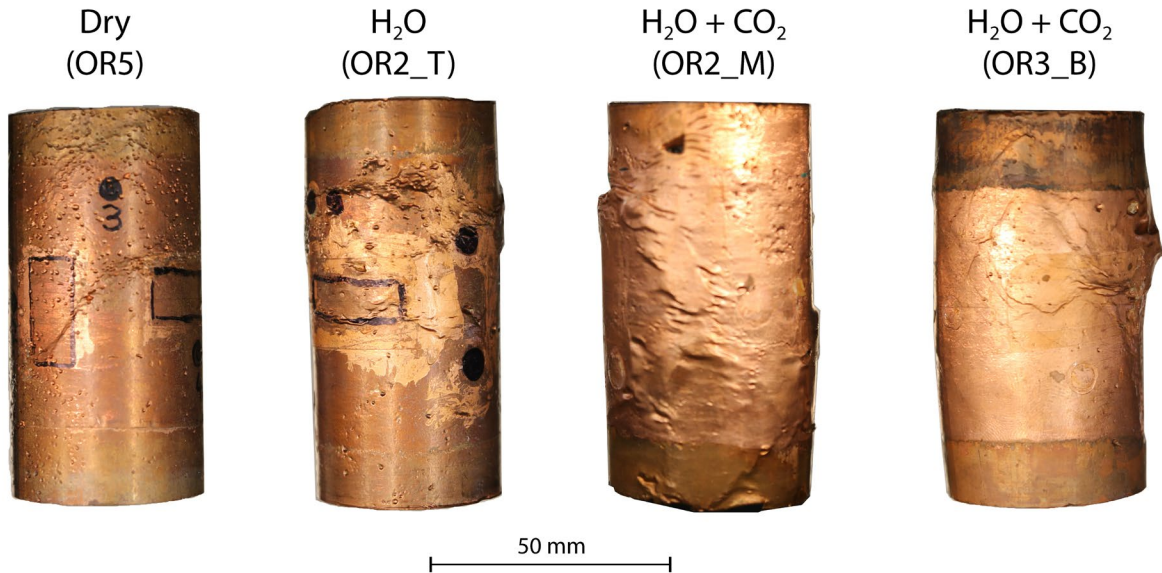
810
811 **Figure A8** Photo of samples after deformation. The dry sample did not reach the final dynamic failure before
812 experiment was halted.

813 **A.6 Elastic Modulus**

814 The Young's modulus (E) of the sample is calculated based on the strain measurement during the elastic loading,
815 using the following equation:

$$816 \qquad E = \frac{\Delta\sigma}{\Delta d/L} \qquad\qquad (\text{Eq. A4})$$

817 where $\Delta\sigma$ is the differential stress, d is the displacement of main ram piston and L is the length of the sample.
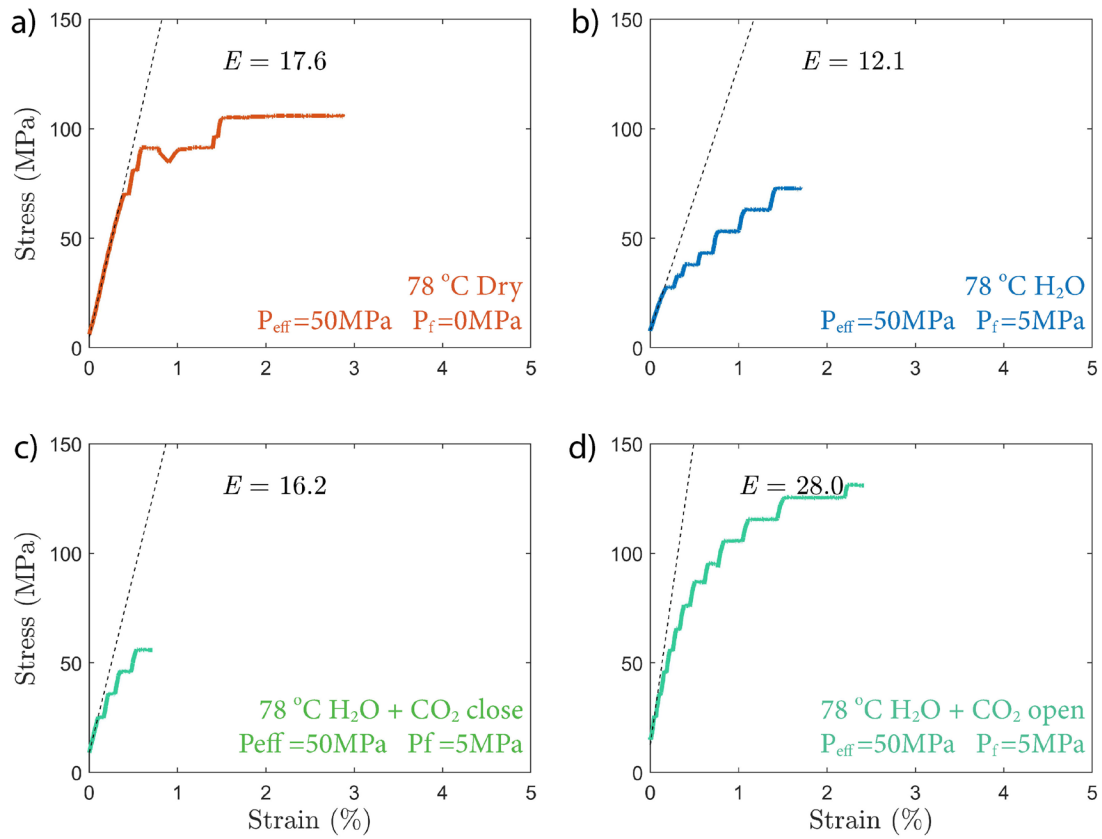
818

819 **Figure A9** Elastic modulus calculated from strain vs stress plots from a) dry, b) H_2O c) H_2O+CO_2 close and d)
820 H_2O+CO_2 open experiments.